

The Pennsylvania State University
The Graduate School
Department of Mechanical and Nuclear Engineering

**AZIMUTHAL HYDROGEN CONCENTRATION FACTOR USING THE
BISON FUEL PERFORMANCE CODE**

A Thesis in
Nuclear Engineering
by
Christopher J. Piotrowski

© 2014 Christopher J. Piotrowski

Submitted in Partial Fulfillment
of the Requirements
for the Degree of

Master of Science

December 2014

The thesis of Christopher Piotrowski was reviewed and approved* by the following:

Arthur Motta
Professor of Nuclear Engineering and Materials Science and Engineering
Chair of Nuclear Engineering
Thesis Advisor

Maria Avramova
Assistant Professor of Nuclear Engineering

Kostadin Ivanov
Distinguished Professor of Nuclear Engineering

Karen A.Thole
Department Head of Mechanical and Nuclear Engineering
Professor of Mechanical Engineering

*Signatures are on file in the Graduate School.

ABSTRACT

Hydrogen can enter nuclear reactors because of the corrosion reaction. Hydrogen that is picked up by nuclear reactor cladding may become heterogeneously distributed due to concentration gradients as described by Fick's law and temperature gradients as described by the Soret effect. Understanding hydrogen behavior is important for ensuring the safety and integrity of a nuclear reactor, since hydrogen that precipitates as hydrides may weaken cladding and lower ductility. This phenomenon has been studied by many researchers since the start of the nuclear industry.

In order to predict hydrogen and hydride distributions, computer codes are essential because of the complexity of models and reactor conditions. A hydrogen transport and precipitation model was created and simulations were previously conducted that predicted the radial and axial distributions of hydrogen and hydrides under various conditions. The current objective of this study and goal of this project is to simulate various azimuthally dependent hydrogen and hydride distributions. This is done through the use of BISON fuel performance that is indirectly coupled to Penn State maintained thermal-hydraulics code, COBRA-TF and the neutronics code, Deterministic Core Analysis based on Ray Tracing (DeCART).

The goal of the azimuthal simulations is to produce boundary condition in which hydrogen and hydride distributions are most heterogeneous. The three simulations highlighted in this study include modeling a 4x4 pin array where a water rod is located near the rod of interest to produce a large thermal gradient, a partially inserted control rod located near the rod of interest to produce a thermal gradient based on differences in power, and modeling cladding in which a portion of the oxide has broken off producing a thermal gradient in the spalled region. A new azimuthal mesh and associated boundaries was created in order to simulate these scenarios. The water rod and control rod simulations used COBRA-TF and DeCART outputs as boundary conditions for the BISON input deck. In each of the simulations, the hydrogen in solid solution

diffused to the colder regions, as anticipated, leading to hydride precipitation in specific favored regions. This resulted in a high concentration in hydride which we believe mimics real cases. Further work can be done to add more competing driving forces to the BISON fuel performance code such as the effect of applied stress on hydrogen and hydride distributions.

TABLE OF CONTENTS

LIST OF FIGURES	vii
LIST OF TABLES	x
ACKNOWLEDGEMENTS	xi
Chapter 1 Background and Introduction.....	1
1.1 Importance of Zirconium Alloys in Nuclear Fuel Cladding	1
1.2 Hydrogen Redistribution and Diffusion in Zirconium Cladding	2
1.3 Corrosion and Hydrogen Pick-up in Zirconium Cladding	6
1.4 Hydride Precipitation and Dissolution in Zirconium Cladding	7
1.5 Motivation of Study	9
1.6 Thesis Outline	10
Chapter 2 Computational Methods.....	12
2.1 Coupled COBRA-TF and DeCART	12
2.1.1 COBRA-TF.....	12
2.1.2 DeCART	14
2.1.3 Coupling.....	17
2.2 BISON Fuel Performance Code.....	18
2.2.1 The Hydrogen Model in BISON	19
2.2.2 Azimuthal Mesh in BISON.....	21
Chapter 3 Simulation Results	24
3.1 Water Rod located near the rod of interest	24
3.2 Control Rod located near the rod of interest	37

3.3 Spallation of Zirconium Oxide	48
Chapter 4 Conclusions and Future Work.....	56
References.....	58

LIST OF FIGURES

Figure 1-1: Measurements of hydrogen diffusion coefficient for Zircaloy-4 [11].	3
Figure 1-2: Radial hydrogen distribution and hydride rim in HBR rod F07 cladding 650 mm above mid-plane (740-wppm H) [13].	4
Figure 1-3: Azimuthal variations of the hydride distribution [13].	6
Figure 1-4: Illustration of the hydride dissolution-precipitation hysteresis [18].	8
Figure 2-1: Computer code coupling scheme [23].	17
Figure 2-2: Azimuthal mesh used for BISON simulations.	22
Figure 2-3: Azimuthal separation of the fuel rod and cladding.	23
Figure 3-1: 4x4 pin water rod simulation schematic with associated enrichments.	25
Figure 3-2: 4x4 pin water rod simulation schematic with beginning of cycle outer cladding temperatures at 0 burnup ($^{\circ}\text{C}$).	25
Figure 3-3: Total linear heat rate for the rod of interest.	27
Figure 3-4: Azimuthal cladding temperature distribution (in degrees K) after 1 hour.	29
Figure 3-5: Azimuthal distribution of hydrogen in solid solution (wt.ppm) in the cladding after 1 hour.	29
Figure 3-6: Azimuthal hydride distribution (wt.ppm) in the cladding after 1 hour.	30
Figure 3-7: Azimuthal cladding temperature distribution (in degrees K) after 1 day.	31
Figure 3-8: Azimuthal cladding temperature distribution (in degrees K) after 7 days.	31
Figure 3-9: Azimuthal cladding temperature distribution (in degrees K) after 1 year.	32
Figure 3-10: Azimuthal distribution of hydrogen in solid solution (wt.ppm) in the cladding after 1 day.	33
Figure 3-11: Azimuthal hydride distribution (wt.ppm) in the cladding after 1 day.	33
Figure 3-12: Azimuthal distribution of hydrogen in solid solution (wt.ppm) in the cladding after 7 days.	35

Figure 3-13: Azimuthal hydride distribution (wt.ppm) in the cladding after 7 days.	35
Figure 3-14: Azimuthal distribution of hydrogen in solid solution (wt.ppm) in the cladding after 1 year.....	36
Figure 3-15: Azimuthal hydride distribution (wt.ppm) in the cladding after 1 year.....	36
Figure 3-16: 4x4 pin assembly with control rod schematic with associated enrichments.	37
Figure 3-17: 4x4 pin water rod simulation schematic with beginning of cycle outer cladding temperatures at 0 burnup (°C).....	38
Figure 3-18: Total linear heat rate for the rod of interest.....	39
Figure 3-19: Azimuthal cladding temperature distribution (in degrees K) after 1 day.....	40
Figure 3-20: Azimuthal hydrogen in solid solution distribution (wt.ppm) in the cladding after 1 day.....	41
Figure 3-21: Azimuthal hydride distribution (wt.ppm) in the cladding after 1 day.....	41
Figure 3-22: Azimuthal cladding temperature distribution (in degrees K) after 1 week.	42
Figure 3-23: Azimuthal cladding temperature distribution (in degrees K) after 33 days.	43
Figure 3-24: Azimuthal cladding temperature distribution (in degrees K) after 66 days.	43
Figure 3-25: Azimuthal hydrogen in solid solution distribution (wt.ppm) in the cladding after 7 days.	44
Figure 3-26: Azimuthal hydride distribution (wt.ppm) in the cladding after 7 days.	45
Figure 3-27: Azimuthal hydrogen in solid solution distribution (wt.ppm) in the cladding after 33 days.	46
Figure 3-28: Azimuthal hydride distribution (wt.ppm) in the cladding after 33 days.	46
Figure 3-29: Azimuthal hydrogen in solid solution distribution (wt.ppm) in the cladding after 66 days.	47
Figure 3-30: Azimuthal hydride distribution (wt.ppm) in the cladding after 66 days.	47
Figure 3-31: Schematic of thermal resistance calculation	48
Figure 3-32: Azimuthal cladding temperature distribution after 1 day in Kelvin.....	50

Figure 3-33: Azimuthal hydrogen in solid solution distribution (wt.ppm) in the cladding after 1 day.....	51
Figure 3-34: Azimuthal hydride distribution (wt.ppm) in the cladding after 1 day.....	52
Figure 3-35: Azimuthal cladding temperature distribution (in degrees K) after 1 year.....	52
Figure 3-36: Azimuthal hydrogen in solid solution distribution (wt.ppm) in the cladding after 30 days.....	53
Figure 3-37: Azimuthal hydride distribution (wt.ppm) in the cladding after 30 days.	54
Figure 3-38: Azimuthal hydrogen in solid solution distribution (wt.ppm) in the cladding after 1 year.....	54
Figure 3-39: Azimuthal hydrogen as hydrides distribution (wt.ppm) in the cladding after 1 year.	55

LIST OF TABLES

Table 2-1: Glossary of terms used in COBRA-TF [25].....	14
Table 2-2: Glossary of terms used in DeCART [26]	16
Table 3-1: Parameters used in CTF and DeCART in the 4x4 water rod near the rod of interest simulation.....	26

ACKNOWLEDGEMENTS

I would like to thank my advisor, Arthur Motta, for his help and guidance throughout my graduate school experience at The Pennsylvania State University. The opportunity was extremely rewarding and he taught me a lot about conducting research, writing academic papers, and thinking about problems from a physical and mathematical point of view. The amount of support Dr. Motta provided me was tremendous. Next, I want to thank Maria Avramova and Kostadin Ivanov for treating me as one of their own students and essentially acting as my second and third advisors. I have had a close relationship with them ever since my undergraduate studies at The Pennsylvania State University. The collaborative research was a very fulfilling experience and helped me learn about the neutronics, thermal-hydraulics and nuclear materials aspects of nuclear engineering at the same time.

Many thanks go to Ian Davis and Olivier Courty for mentoring me during the early stages of my project. Ian Davis provided a lot of help explaining how to use BISON. Often times when something didn't make sense or wouldn't work as intended, Ian was there to answer any questions, even after getting a job. I do not know where I would be without the help of Olivier Courty. Our collaborative work over the summer was one of my most unforgettable experiences during my graduate studies.

Thank you to Christopher Dances and Michael Mankosa. I had the pleasure of working very closely with both individuals as research partners. Christopher Dances greatly helped me become accustomed to using Linux software. Working directly with Michael Mankosa was an amazing experience. His work ethic made him an excellent research partner. I wish them both the very best with their graduate studies.

I wanted to thank the United States Department of Energy for providing financial support for the project through the NEUP project 11-2987. I also wanted to thank Jason Hales, Shane

Stafford, the BISON group and the staff at Idaho National Lab for their help and strong support with using BISON fuel performance code. When something went wrong with BISON, Michael Mankosa and I often found ourselves looking to Shane Stafford for guidance and for this I would like to give special thanks.

At The Pennsylvania State University, I want to thank all of my friends, professors, and the students of the Nuclear Materials Groups. Thank you to everyone for making my experiences at The Pennsylvania State University truly unbelievable. An extra special thanks goes to Jeffrey Zoghby, Jacob Krizmanich and Alex Punzi for helping me with anything I could possibly need and being a great emotional support group.

I would like to thank my parents from the bottom of my heart for their unrelenting support throughout my college experience. Words cannot explain how grateful I am for this opportunity and it goes without saying that I wouldn't be where I am today without their love and support. I also want to thank Daniel Piotrowski and Janina Piotrowski for their endless encouragement and constantly pushing me to be the best that I can be.

Finally, I would like to thank my amazing girlfriend, Maureen Suchecki, for her never ending support and motivation. Without her I am not sure if I would have been able to complete half of my graduate studies. She always seemed to know the best things to say to make sure I was able to push myself to unthinkable limits.

Thank you again to everyone for this amazing experience.

Chapter 1 Background and Introduction

This chapter provides basic knowledge about hydrogen behavior in Light Water Reactor (LWR) fuel cladding. Section 1.1 provides a fundamental background about the importance of zirconium alloys used as nuclear cladding material. The oxidation mechanisms that produce hydrogen in reactor cladding at the cladding-coolant interface are detailed in section 1.2. Section 1.3 explains the factors that affect the redistribution and diffusion of hydrogen within the reactor cladding. Section 1.4 briefly reviews effects of hydrides within the cladding and studies used to model hydride precipitation and dissolution. The purpose and motivation of this study is found in section 1.5. Section 1.6 contains a description of the organization of the thesis.

1.1 Importance of Zirconium Alloys in Nuclear Fuel Cladding

The nuclear industry always aims to improve current commercial nuclear reactors with great focus on extending the lifetime of the nuclear reactor and taking measures to avoid unsafe operation. The materials in a nuclear reactor operate under very high pressures, high temperatures, large thermal gradients, and intense nuclear radiation [1]. Materials that can withstand these dangerous conditions are in high demand. Light Water Reactors contain fuel assemblies that are cooled by water. These fuel assemblies are made up of fuel rods which contain fissile material within the matrix of fuel pellets made of uranium dioxide (UO_2). The fuel pellets are encased in a nuclear fuel cladding tube made of various zirconium alloys which acts as the main barrier to fission product release into the primary circuit coolant. It is important for the cladding material to withstand reactor operating and accident scenarios for extended periods of time while maintaining the integrity of the material. Zirconium alloys are typically chosen because of their low neutron absorption cross-section, low corrosion rates, good heat transfer properties, and some resistance to radiation damage [2, 3]. Much is known about the effect of mechanical and thermal stresses on material behavior; however, there is much to learn about the

nuclear radiation and corrosion behavior. Understanding these phenomenon is vital for improving core structures within a nuclear reactor to their full potential while maintaining safe operation.

Two of the most common zirconium alloys used within the nuclear industry are Zircaloy-2 and Zircaloy-4. These alloys contain small amounts of iron, chromium tin and nickel, in varying weight percentages which can strongly impact the in-service behavior [2]. Zircaloy-4 is often used in Pressurized Water Reactors (PWRs) and Zircaloy-2 used in Boiling Water Reactors (BWRs). Modern alloys, such as ZIRLO and M5, have aroused the industry's interest because they exhibit improved corrosion resistance [4, 5].

1.2 Hydrogen Redistribution and Diffusion in Zirconium Cladding

When hydrogen is absorbed into the cladding, the hydrogen in solid solution may diffuse via two mechanisms. Hydrogen can diffuse due to a temperature gradient, as described by the Soret Effect, or a concentration gradient, as described by Fick's Law. Research has been conducted to find a way to model this behavior particularly by Sawatzky. Sawatzky's article in the Journal of Nuclear Materials describes the diffusion of hydrogen in solid solution as a function of these gradients [8]. The following equation describes the contributions of the Soret Effect and Fick's Law on hydrogen diffusion as described by Sawatzky:

$$J = -D\nabla C - \frac{DCQ^*}{RT^2}\nabla T \quad 1-1$$

Where,

- J = diffusion flux
- D = diffusion coefficient of hydrogen
- C = concentration of hydrogen in solid solution
- R = gas constant
- T = temperature
- Q* = the heat of transport

The first term on the right side of Equation 1-1 describes the flux of hydrogen based on a concentration gradient, Fick's Law. The second term corresponds to the temperature gradient or

Soret Effect. Each individual portion and derivation is found in greater deal within Olivier Courty's Master's thesis [9]. The diffusion coefficient found in both terms is described by an Arrhenius law:

$$D = A_D \exp\left(-\frac{Q_D}{RT}\right) \quad 1-2$$

Where,

R is the gas constant

T is the temperature in Kelvin

and the coefficients were found by Kearns to be [10]:

$$A_D = 7.90 \times 10^{-7} \frac{m^2}{s} \quad 1-3$$

$$Q_D = 4.49 \times 10^4 \frac{J}{mol} \quad 1-4$$

Kammenzind compiled the most used correlations for the diffusion coefficient and can be found in Figure 1-1.

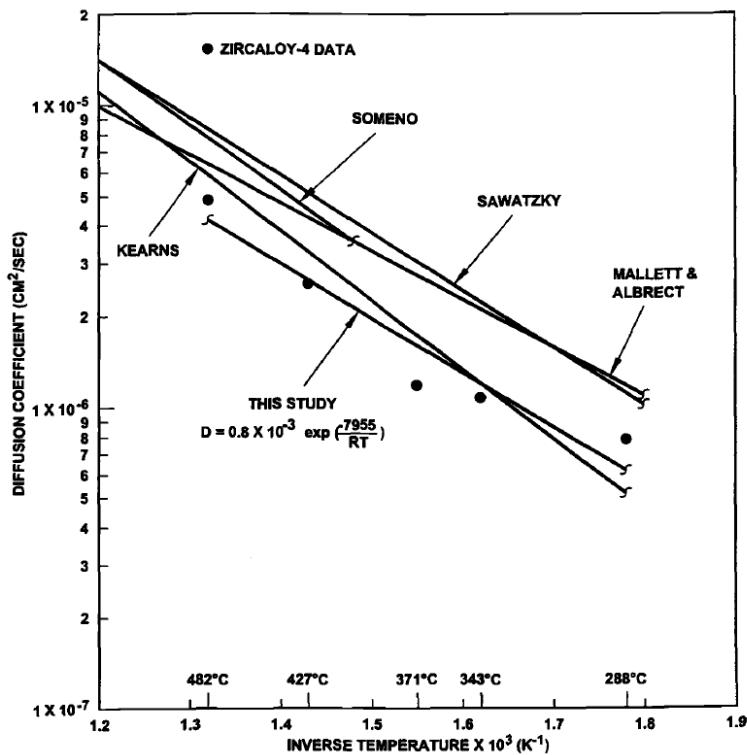


Figure 1-1: Measurements of hydrogen diffusion coefficient for Zircaloy-4 [11].

As more hydrogen is picked up into the cladding, the first term on the right side in Equation 1-1 means that the concentration gradient will drive the hydrogen from a region of high concentration to a region of low concentration. Since hydrogen is picked up at the outer cladding and coolant interface, the hydrogen will diffuse further into the cladding. The second term in Equation 1-1 also results in a hydrogen flux, since the temperature gradient in the fuel rod can vary in all directions radially, axially, and azimuthally. Radially, the fuel pellet generates heat while the coolant acts as a heat sink. This creates a radial temperature distribution. A temperature drop of approximately 30 °C is observed across the cladding [12]. The effect of this temperature distribution can be seen by the formation of a hydride rim near the cladding-coolant interface. Figure 1-2 shows the radial hydrogen distribution and hydride rim.

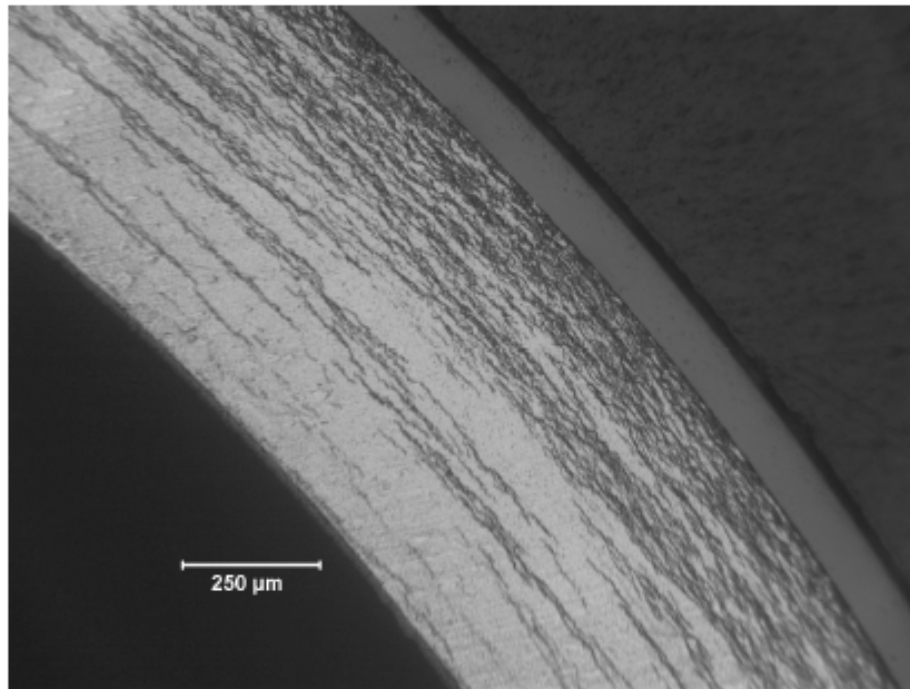


Figure 1-2: Radial hydrogen distribution and hydride rim in HBR rod F07 cladding 650 mm above mid-plane (740-wppm H) [13].

Axially, in a PWR coolant enters the core at a temperatures of about 287 °C and exits at about 320 °C [12]. This axial temperature gradient in the coolant would tend to cause an axial temperature gradient within the cladding and the corrosion is higher in the upper grid spaces. Fuel pellets are manufactured with dishes and chamfers to allow space for fission gas release, thermal expansion and swelling. With less fuel and consequently less energy deposition, there is an axial temperature gradient along the inter-pellet gaps. Hydrogen diffuses towards the cold regions that the inter-pellet gaps create however there are very few measurements of the axial distribution of hydrogen as a function of elevation [14].

Azimuthally, temperature gradients can be produced due to geometric heterogeneity in the fuel rod arrangement. An example of this geometry is a water rod placed next to a fuel rod, since in this case one side of the fuel rod is exposed to more moderation than the other side surrounded by fuel rods. This geometry would cause a temperature gradient for the hydrogen to follow. Other examples include replacing the water rod with a control rod, different locations within the assembly (edges, corners, near spacers, etc.) and defects in the cladding such as the spallation of oxide, which can all create heterogeneous temperature distributions that affect the hydrogen distribution. The goal of this thesis is to explore various examples of azimuthal hydrogen distribution and to create simulations that follow this phenomenon. Figure 1-3 shows a collection of irradiated cladding metallography produced by Billone et al. that depicts a heterogeneous hydrogen distribution from a ZIRLO sample exposed to temperature less than or equal to 1200 °C at 2910 mm from the rod bottom.

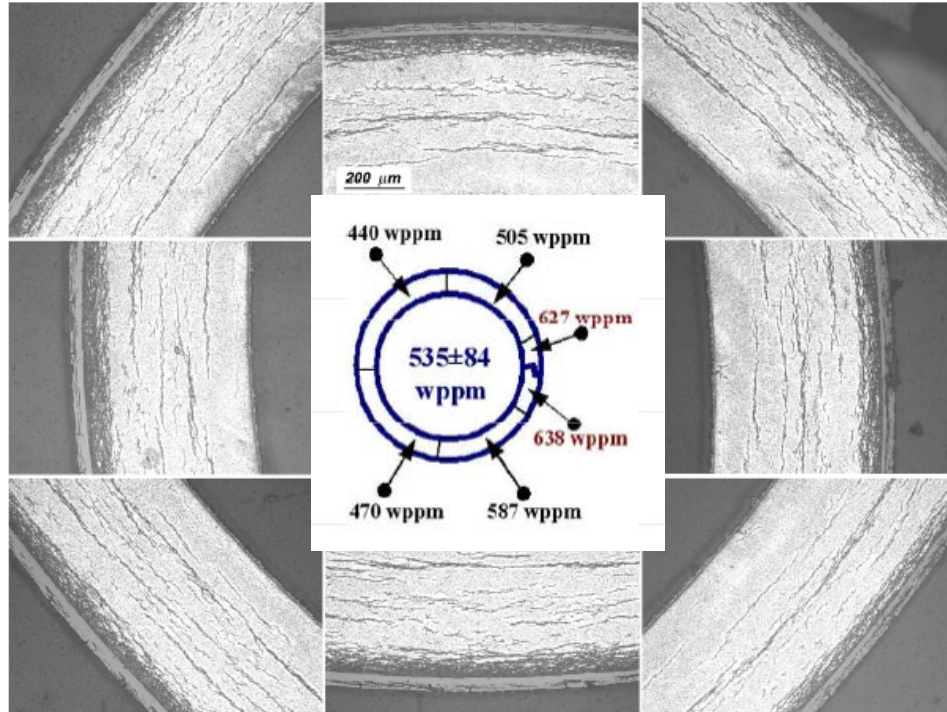


Figure 1-3: Azimuthal variations of the hydride distribution [13].

1.3 Corrosion and Hydrogen Pick-up in Zirconium Cladding

Under normal reactor operating conditions, zirconium cladding is exposed to temperature ranges of 330-380 °C at the outer surface and inner surface respectively. The outer surface of the zirconium cladding is in contact with the coolant water. This interface interaction causes a corrosion reaction which generates hydrogen:



A fraction of the hydrogen produced in the above reaction is picked up by the cladding (approximately 10-20%) [6]. The corrosion reaction degrades the fuel cladding and creates a protective zirconium oxide layer on the outer surface of the cladding, which can act as a thermal

resistance. Some other notable sources of hydrogen are hydrogen generated by radiolysis and hydrogen intentionally added to the coolant to limit oxidation [7].

1.4 Hydride Precipitation and Dissolution in Zirconium Cladding

Over time as an increasing amount of hydrogen enters the cladding, the concentration of hydrogen in solid solution approaches the Terminal Solid Solubility for precipitation (TSSp) [15, 16]. Hydrogen in solid solution precipitates into hydrides when the concentration is above this limit. Understanding the distributions of hydrogen in solid solution and hydrides is important because they are linked to reduced cladding ductility, and increase the chance of cladding failure [17].

The Terminal Solid Solubility has been determined by various authors, including Kearns and McMinn [15, 16]. Kearns described a diffusion couple experiment that approximated the TSS for Zircaloy-2 and Zircaloy-4 for low concentrations of hydrogen (50-160 wt. ppm) at temperatures below 550 °C [15]:

$$TSSp(wt. ppm) = 1.2 \times 10^5 \exp\left(-\frac{4302}{T}\right) \quad 1-6$$

Where T = temperature in Kelvin

The hysteresis phenomenon observed between the dissolution and precipitation Terminal Solid Solubility was studied by McMinn using Kearns' study as a foundation [16]. The TSS for dissolution (TSSd) and the TSS for precipitation (TSSp) were found to occur at different temperatures. This temperature hysteresis is a result of the work associated with volume expansion which is required for hydride precipitation, as illustrated in Figure 1-4.

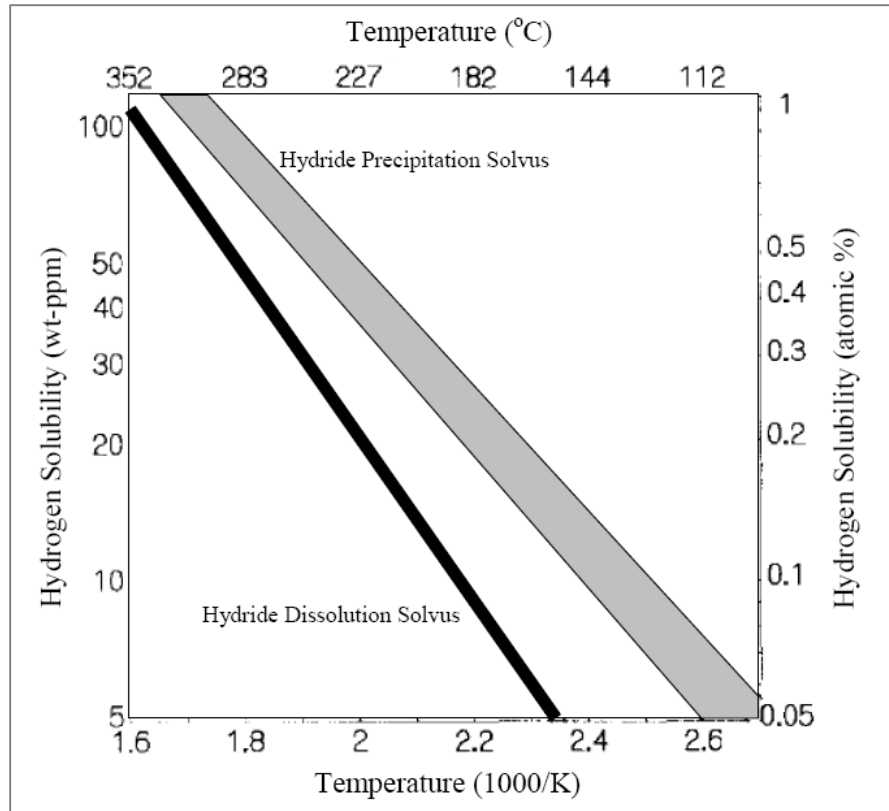


Figure 1-4: Illustration of the hydride dissolution-precipitation hysteresis [18].

McMinn found the TSS for dissolution and TSS for precipitation in Zircaloy 4 as:

$$\begin{cases} TSSd \text{ (wt. ppm)} = 106446.7 * \exp\left(-\frac{4328.67}{T \text{ (K)}}\right) \\ TSSp \text{ (wt. ppm)} = 138746.0 * \exp\left(-\frac{4145.72}{T \text{ (K)}}\right) \end{cases} \quad 1-7$$

With these equations, the steady state hydride concentration in a given sample can be estimated.

The precipitation of hydrogen in solid solution to hydrides does not occur instantly. The kinetics of this change was modeled by Marino [19]:

$$\frac{dC}{dt} = -\nabla J - \alpha^2(C - TSSp) \quad 1-8$$

Where,

C = concentration of hydrogen in solid solution

J = the diffusion flux

α = precipitation rate constant

TSSp = Terminal Solid Solubility Limit for precipitation

A detailed derivation and explanation of the precipitation rate constant can be found in Olivier Courty's Master's thesis [9].

1.5 Motivation of Study

As mentioned in previous sections, zirconium is a very important material that is used in the fuel cladding as a first barrier against the release of fission gasses within the fuel rod. Ensuring that this protective barrier can withstand reactor conditions for extended periods of time is vital for the safety of the reactor. The hydrogen pickup during operation is one of the limiting factors of the integrity of the cladding. When hydrogen is picked up in the cladding, the hydrogen diffuses based on temperature and concentration gradients, and if the hydrogen content reaches the solubility limit the hydrogen precipitates as zirconium hydrides. These brittle hydrides have been shown to induce a loss of cladding ductility [20]. Understanding and modelling hydrogen and hydride behavior can help to identify regions of high hydrogen concentrations within the cladding, which would be likely to fail.

This study is aimed at exploring the anisotropic azimuthal power and temperature distribution on fuel rods and its impact on hydride distribution. Previous work has been done by Olivier Courty to create a hydrogen model that accurately predicts hydrogen and hydride distributions within BISON fuel performance code [21]. BISON fuel performance code was also coupled to neutronics (DeCART) and thermal-hydraulics codes (CTF) [22]. An investigation of the axial and radial hydrogen distributions were modeled and reported in Olivier Courty and Ian Davis's theses [9, 23].

The main purpose of this study is to explore various azimuthal configurations using the previously mentioned coupled codes to produce temperature distributions that can affect hydrogen and hydride distribution. Three simulations have been chosen for this investigation to provide a variety of hydrogen distributions. The first case is the spallation of the oxide layer which may occur at high burnup. When the oxide spall occurs, a portion of the oxide on the fuel cladding breaks off creating a cooler spot under which a hydrogen blister can form [24]. The second and third cases involve placing a water and control rod next to the rod of interest respectively. The water rod provides extra moderation to one side of the fuel rod creating a temperature gradient along the azimuth. Finally, the control rod provides a heterogeneous power distribution which in turn creates a heterogeneous azimuthal temperature distribution which also results in a heterogeneous hydrogen and hydride distribution. The goal of these simulations is to identify their high risk areas due to the hydrogen redistribution.

1.6 Thesis Outline

This section describes the outline of the thesis. For a detailed list of section titles and associated page numbers, please refer to the Table of Contents beginning on page V. Chapter 1 explains background information in detail and introduces the topics described in this thesis. The motivation for this work is also explained with support from literature. Chapter 2 describes the computer codes used for this project. The chapter begins by explaining some of the functionality of the thermal-hydraulics code (COBRA-TF) followed by the neutronics code (DeCART) used in this project. The next section briefly describes the coupling scheme between COBRA-TF, DeCART and the fuel performance code (BISON) along with subsequent information relayed between codes. Chapter 2 concludes with an explanation of BISON and how an azimuthal mesh was created for specific simulations. Chapter 3 describes the results found for multiple azimuthally heterogeneous simulations. The chapter begins by describing the results found from simulating a water rod near the rod of interest. Next, the results from a partially inserted control

rod were reported. Finally, the spallation of zirconium oxide and the effects on hydrogen and hydride distributions conclude chapter 3. Chapter 4 discusses the conclusions and potential future work that may come from this study. References and appendices can be found at the end of the thesis.

Chapter 2 Computational Methods

Computer codes are very important in the nuclear industry to assess conditions which cannot be tested in nuclear reactors but that can limit the reactor's performance. Obtaining experimental data from a reactor core can be very expensive both from a cost and time perspective. Computer codes provide a safer, more efficient way to study and confirm the safety of a reactor. Many accident scenarios and operating conditions can be simulated in order to predict the behavior of a reactor under these conditions. Within this study, three computer codes were used, including COBRA-TF, DeCART, and BISON. In this study these codes are used in a manner that combines their strengths to more accurately simulate reactor conditions. Section 2.1 briefly discusses the capabilities of COBRA-TF and DeCART as well as their direct coupling. Section 2.2 discusses the capabilities of BISON and of the hydrogen model used for this study.

2.1 Coupled COBRA-TF and DeCART

2.1.1 COBRA-TF

COBRA-TF (CTF) is a thermal-hydraulics code that utilizes two-fluid, three-field subchannel analysis. CTF was developed and is maintained at Penn State University [25]. The strengths of thermal hydraulics codes lie in the heat transfer and fluid mechanics calculations particularly within the coolant. CTF uses three conservation equations to simulate reactor thermal-hydraulics: conservation of mass, momentum and energy [25]. A glossary of terms for these equations can be found at the end of this section. Equation 2-1 is the mass conservation equation used by CTF.

$$\frac{\partial}{\partial t}(\alpha_k \rho_k) + \nabla \cdot (\alpha_k \rho_k \vec{V}_k) = L_k + M_e^T \quad 2-1$$

In COBRA-TF, k is a subscript representing the type of phase field. $\frac{\partial}{\partial t}(\alpha_k \rho_k)$ is the change of mass with respect to time. $\nabla \cdot (\alpha_k \rho_k \vec{V}_k)$ is the advection of the field mass into or out of the volume. \vec{V} is the field velocity. L_k represents the mass transfer into or out of phase k ; modes of inter-phase mass transfer include evaporation/condensation and entrainment/de-entrainment. M_e^T is the entrained droplet mass source term due to turbulent mixing. Equation 2-2 is the conservation of momentum used by CTF.

$$\begin{aligned} & \frac{\partial}{\partial t}(\alpha_k \rho_k \vec{V}_k) + \frac{\partial}{\partial x}(\alpha_k \rho_k u_k \vec{V}_k) + \frac{\partial}{\partial y}(\alpha_k \rho_k v_k \vec{V}_k) + \frac{\partial}{\partial z}(\alpha_k \rho_k w_k \vec{V}_k) \\ & = \alpha_k \rho_k \vec{g} - \alpha_k \nabla P + \nabla \cdot [\alpha_k (\tau_k^{ij} + T_k^{ij})] + \vec{M}_k^L + \vec{M}_k^d + \vec{M}_k^T \end{aligned} \quad 2-2$$

$\frac{\partial}{\partial t}(\alpha_k \rho_k \vec{V}_k)$ is the change of volume momentum with time. $\frac{\partial}{\partial x}(\alpha_k \rho_k u_k \vec{V}_k) + \frac{\partial}{\partial y}(\alpha_k \rho_k v_k \vec{V}_k) + \frac{\partial}{\partial z}(\alpha_k \rho_k w_k \vec{V}_k)$ represent the advection of momentum in the Cartesian direction. $\alpha_k \rho_k \vec{g}$ represents the gravitational force, $\alpha_k \nabla P$ the pressure force, $\nabla \cdot [\alpha_k (\tau_k^{ij} + T_k^{ij})]$ the viscous and turbulent shear stress, \vec{M}_k^L is the momentum source/sink due to phase change and entrainment, \vec{M}_k^d is the interfacial drag forces, and \vec{M}_k^T is the momentum transfer due to turbulent mixing. The turbulent shear stress is present in Equation 2-2, but it is not modeled in CTF. The final conservation equation used in CTF is the conservation of energy.

$$\frac{\partial}{\partial t}(\alpha_k \rho_k h_k) + \nabla \cdot (\alpha_k \rho_k h_k \vec{V}_k) = -\nabla \cdot [\alpha_k (\vec{Q}_k + \vec{q}_k^T)] + \Gamma_k h_k^i + q_{wk}''' + \alpha_k \frac{\partial P}{\partial t} \quad 2-3$$

$\frac{\partial}{\partial t}(\alpha_k \rho_k h_k)$ is the change in phase energy with respect to time, and $\nabla \cdot (\alpha_k \rho_k h_k \vec{V}_k)$ is the advection of phase energy into or out of the cell. $\nabla \cdot [\alpha_k (\vec{Q}_k + \vec{q}_k^T)]$ is the k -phase conduction and turbulent heat flux, $\Gamma_k h_k^i$ is the energy transfer due to phase-change, q_{wk}''' is the volumetric wall heat transfer, and $\alpha_k \frac{\partial P}{\partial t}$ is the pressure work term. The purpose of using CTF is to obtain an

accurate cladding temperature distribution (r, θ, z) that will later be inputted into BISON and will serve as one of the driving forces for hydrogen redistribution. Further explanation of the capabilities and theory for CTF can be found in the CTF Theory Manual [25].

Table 2-1: Glossary of terms used in COBRA-TF [25]

Term	Definition
α_k	Average-k phase void fraction
ρ_k	Average k-phase density
V_k	Field velocity
L_k	Mass transfer into or out of phase k
M_e^T	Entrained droplet mass source term due to turbulent mixing
u_k	Average k-phase velocity in the x Cartesian direction
v_k	Average k-phase velocity in the y Cartesian direction
w_k	Average k-phase velocity in the z Cartesian direction
\vec{g}	Acceleration of gravity
P	Average pressure
τ_k^{ij}	Viscous shear stress tensor
T_k^{ij}	Turbulent shear stress tensor
\vec{M}_k^T	Momentum transfer due to turbulent mixing
\vec{M}_k^d	Interfacial drag forces
\vec{M}_k^L	Momentum source/sink due to phase change and entrainment
h_k	Average k-phase enthalpy
\vec{Q}_k	Average k-phase conduction vector
\vec{q}_k^T	Average k-phase turbulent heat flux
Γ_k	Average rate of vapor generation per unit volume
h_k^i	Surface average k-phase enthalpy
q_{wk}'''	Interfacial heat transfer in the k-phase

2.1.2 DeCART

The Deterministic Core Analysis based on Ray Tracing code or DeCART was developed by KAERI as part of a United States – Republic of Korea (US-ROK) collaborative National Energy Research Institute (I-NERI) project between KAERI, ANL, and Purdue University [26]. DOE, the *Electric Power Research Institute* (EPRI), and Advanced Fuel Cycle Initiative (AFCI) have supported its further development in the United States [26]. DeCART is a neutronics code based on the method of characteristics (MOC) capable of modeling from single-pin models to full-core calculations of 3D neutron flux. Neutronics codes rely on accurate cross section

generation and fission energy deposition calculations to calculate the neutron flux [26]. Input parameters include geometry, material composition, thermal operating conditions, and program execution control parameters [26]. DeCART solves the integral transport equation using the method of characteristics (MOC) approach with discrete ray tracing [26]. Hursin, one of the authors of the DeCART Theory Manual, notes that the direct application of MOC to fully 3-D core models is computationally expensive [26]. For the planar directions, the 2-D MOC approach is applied to the Boltzmann transport equation in steady-state, given in Equation 2-4.

$$\Omega \cdot \nabla \varphi(r, \Omega, E) + \Sigma(r, E)\varphi(r, \Omega, E) = q(r, \Omega, E) \quad 2-4$$

With the assumption of an isotropic fission source, the source term can be written as:

$$\begin{aligned} q(r, \Omega, E) &= \frac{1}{4\pi} \frac{\chi(r, E)}{k} \int_0^\infty dE' v \Sigma_f(r, E') \varphi(r, E') \\ &+ \int_0^\infty dE' \int_{4\pi} d\Omega' \Sigma_s(r, \Omega' \rightarrow \Omega, E' \rightarrow E) \varphi(r, \Omega', E') \end{aligned} \quad 2-5$$

In Equations 2-4 and 2-5, $\varphi(r, \Omega, E)$ represents the angular flux per unit volume, per solid angle, and per energy. The scalar flux can be found by integrating the angular flux over the solid angle, shown in Equation 2-6.

$$\phi(r, E) = \int_{4\pi} \varphi(r, \Omega, E) d\Omega \quad 2-6$$

Equation 2-7 shows this expression which will serve as the basic equation for determining angular flux with MOC.

$$\bar{\varphi}(r_r, \Omega_r, E) = \bar{\varphi}(r_{r,0}, \Omega_r, E) \exp\left(-\frac{\bar{\Sigma}(E)s}{\sin \theta}\right) + \frac{\bar{q}(\Omega_r, E)}{\Sigma(E)} \left[1 - \exp\left(-\frac{\bar{\Sigma}(E)s}{\sin \theta}\right)\right] \quad 2-7$$

The LHS of Equation 2-7 represents the axially integrated angular flux for a computational plane of arbitrary thickness. To solve for the angular and scalar fluxes, DeCART divides the problem into N flat source regions. Next the multi-group formulation is used to separate the energy dependence into g energy groups. Using this discretization, the angular flux is shown in Equation 2-8.

$$\varphi_{l,m}^g(r) = \Delta\alpha \int_{E_{g+1}}^{E_g} \bar{\varphi}(r, \alpha_l, \theta_m, E) dE \quad 2-8$$

α_l is the azimuthal angle and θ_m is the polar angle, which together make up the solid angle, $\Omega(\alpha_l, \theta_m)$. g represents the energy group, and not shown is the notation, n, which represents the flat source region. With the average flux distribution, DeCART applies the 1-D multi-group diffusion equation. Once solved, the solution to the diffusion equation and flux equation are used in the NEM equation to obtain node averaged fluxes. Finally, the 1-D NEM solution and 2-D MOC solution are coupled together through transverse leakage terms [26]. This neutronics code solves for local power distributions which will be utilized by the fuel performance code BISON as a boundary condition. Further explanation of the capabilities and theory for DeCART can be found in the DeCART Theory Manual [26].

Table 2-2: Glossary of terms used in DeCART [26]

Term	Definition
Ω	Solid angle
φ	Angular flux distribution
r	Radial direction
E	Energy
Σ	Macroscopic cross-section
q	Fission and scattering source term
χ	Probability of a fission being born
k	Reactivity
v	Neutron speed
Σ_f	Macroscopic fission cross-section
ϕ	Scalar flux
Σ_s	Macroscopic scattering cross-section
α, α_1	Azimuthal angle
E_g	Energy in group g
θ_m	Polar angle

2.1.3 Coupling

In order to more accurately simulate a reactor it is best to couple codes together in order to capture the influence of thermal-hydraulic conditions with neutronics and vice-versa. This was done within this project as the Master's thesis for Ian Davis at Penn State University and further altered by Michael Mankosa and Christopher Dances to allow for azimuthal variation of the neutron flux and properties [23]. CTF and DeCART were externally coupled together with bi-directional feedback, a more detailed description of procedure used to produce this coupling can be found in [23]. Once CTF solves for the cladding temperature distribution and DeCART solves for the power distribution, this information is stored in a CSV file which can then be inputted into BISON. Figure 2-1 shows the computer code coupling scheme used with input and output information shown by the arrows.

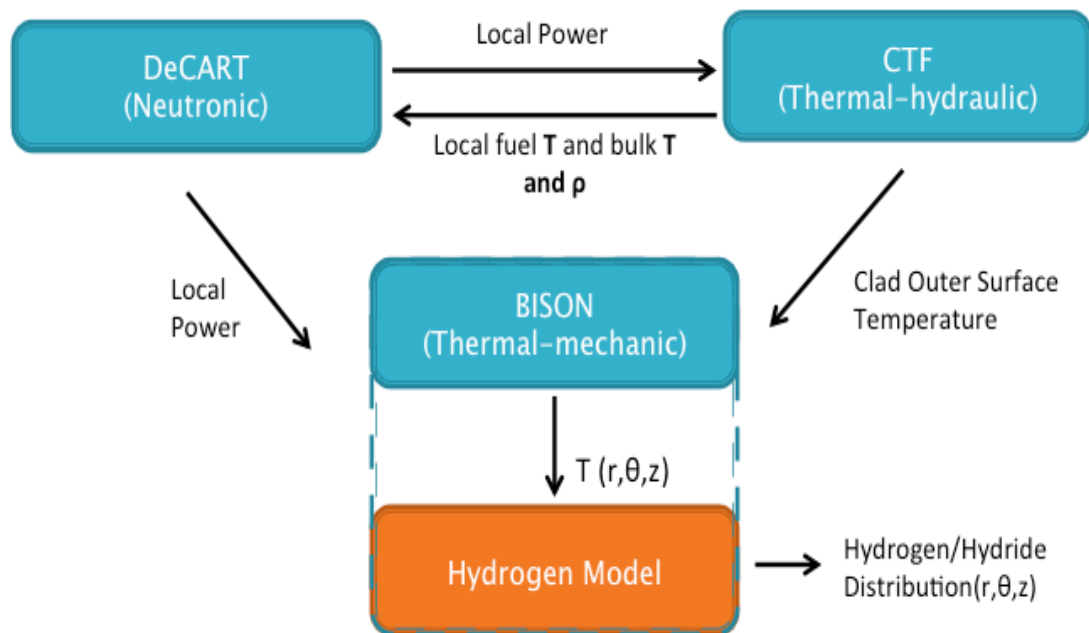


Figure 2-1: Computer code coupling scheme [23].

2.2 BISON Fuel Performance Code

In order to predict the hydrogen distribution, a fuel performance code developed by Idaho National Laboratory called BISON is used [27]. BISON is a finite-element based nuclear fuel performance code applicable to a variety of materials including light water reactor fuel rods, TRISO particle fuel, and metallic rod/ plate fuel. BISON is built on a complex mathematics solver known as MOOSE, Multiphysics Object Oriented Simulation Environment [27]. Regarding specific models in BISON, there are a number of governing equations to define the conservation of mass, momentum, and energy. First the conservation of energy is given in terms of heat conduction in Equation 2-9.

$$\rho C_p \frac{\partial T}{\partial t} + \nabla \cdot \mathbf{q} - E_f \dot{F} = 0 \quad 2-9$$

T is the temperature, ρ is the density, C_p is the specific heat, \mathbf{q} is the heat flux, E_f is the energy released by a single fission event; \dot{F} is the volumetric fission rate. The heat flux due to thermal conductivity represented by \mathbf{q} is shown in Equation 2-10.

$$\mathbf{q} = -k\nabla T \quad 2-10$$

Where,

k is the material thermal conductivity. Next, the conservation of mass equation is shown in Equation 2-11.

$$\frac{\partial C}{\partial t} + \nabla \cdot \mathbf{J} + \lambda C - S = 0 \quad 2-11$$

C is the concentration, \mathbf{J} is the mass flux, λ is the radioactive decay constant, and S is the source rate for a given species.

Finally, the conservation of momentum is given by Equation 2-12.

$$\nabla \cdot \sigma + \rho f = 0 \quad 2-12$$

σ is the Cauchy stress tensor, ρ is the density, and f represents the body force per unit mass [28].

Using these equations a three-dimensional temperature distribution within a reactor fuel rod can be calculated. It can be seen from Figure 2-1 that there is no feedback from the BISON fuel performance code (the coupling is only one way). Once the input files are created and referenced by BISON, the BISON fuel performance code is run using a hydrogen model with temperature and hydrogen/hydride distribution calculated as outputs. This will be further explored in the next section.

2.2.1 The Hydrogen Model in BISON

BISON requires certain boundary conditions from other codes to run a fuel performance simulation. These boundary conditions come from CTF and DeCART. As mentioned previously, CTF provides BISON with the outer cladding temperature distribution while DeCART provides a power distribution in the fuel pellet. Internally, BISON contains the Dittus-Bolter correlation, which can calculate convective heat transfer coefficient, which yields the outer cladding temperature. This is important for one of the later simulations that does not receive a cladding temperature distribution from CTF. CTF contains information about the two-fluid flow and cross-flow heat transfer when using the subchannels themohydraulics. Therefore, CTF is used to generate the outer clad temperature profile for BISON. In addition to the temperature boundary conditions, BISON requires fission rates in its calculations. One way to provide these fission rates is by specifying a linear heat rate combined with an axial power shape. Both parameters are calculated as a function of time, and then converted to a fission rate as a function of space using a

constant value of energy per fission. As mentioned previously, both sets of boundary conditions are generated from coupled CTF-DeCART calculations.

From the precipitation, dissolution and diffusion equations described in Chapter 1, the balance equation for hydrogen in solid solution and hydride concentration can be deduced. The variation of hydrogen in solid solution per unit time is given by the sum of the net flux, the hydrogen created by the dissolution of hydride minus the hydrogen transformed into hydrides due to precipitation.

Four different cases have to be taken into account for the writing of the balance equations of the hydrogen model as described in [9] and summarized below:

In the first case, the concentration of hydrogen in solid solution is greater than the TSSp. Then, precipitation occurs according to the laws described above.

- Precipitation:

$$if C_{ss} > TSSp, \left\{ \begin{array}{l} \frac{dC_{ss}}{dt} = -\nabla \cdot J - \alpha^2 (C_{ss} - TSSp) \\ \frac{dC_p}{dt} = \alpha^2 (C_{ss} - TSSp) \end{array} \right\} \quad 2-13$$

In the second case, the concentration in solid solution is between the TSSd and the TSSp. This is the “hysteresis” area, where neither dissolution nor precipitation occurs.

- Hysteresis:

$$if TSSp \geq C_{ss} > TSSd, \left\{ \begin{array}{l} \frac{dC_{ss}}{dt} = -\nabla \cdot J \\ \frac{dC_p}{dt} = 0 \end{array} \right\} \quad 2-14$$

In the third case, the concentration in solid solution is below the TSSd. The hydrogen in the precipitated hydrides (C_p) is dissolving so that the C_{ss} matches the TSSd value. This is possible only if there are hydrides ($C_p > 0$).

- Dissolution:

$$\text{if } TSSd \geq C_{ss} \text{ and } C_p > 0 \text{ and } \nabla J > 0$$

$$\text{then } \left\{ \begin{array}{l} \frac{dC_{ss}}{dt} = -\nabla \cdot J + \beta^2(TSSd - C_{ss}) \\ \frac{dC_p}{dt} = -\beta^2(TSSd - C_{ss}) \end{array} \right\} \quad 2-15$$

In the fourth and last case, the concentration in solid solution is below the TSSd but there are no more hydrides to dissolve. In that case, the only change to hydrogen concentration comes from net diffusion flux.

- Diffusion only:

$$\text{if } TSSd \geq C_{ss} \text{ and } C_p = 0, \left\{ \begin{array}{l} \frac{dC_{ss}}{dt} = -\nabla \cdot J \\ \frac{dC_p}{dt} = 0 \end{array} \right\} \quad 2-16$$

The initial concentrations of the hydrogen in solid solution and hydrogen as hydrides are given as an input parameter into BISON. Using the outer cladding temperature distribution and the fission rates found by inputting the power distribution, BISON is able to predict the hydrogen distribution and subsequently the hydride distribution at all timesteps. This model was used in order to predict the axial and radial temperature and hydrogen/ hydride distributions [9, 23]. The purpose of this study is to further simulate azimuthal sections of a fuel rod and obtain the temperature, hydrogen and hydride distributions in conditions where large variations in azimuthal hydrogen distribution should be expected.

2.2.2 Azimuthal Mesh in BISON

Previously, this project was able to use a meshing script available on the BISON server. This script created a mesh in the radial and axial directions and associated boundaries. This meshing script was not capable of producing an azimuthal mesh for the purpose of heterogeneous

reactor conditions. For this reason, a new mesh and associated boundaries was created using CUBIT/Trellis software. Figure 2-2 shows the mesh used in BISON for azimuthal dependence.

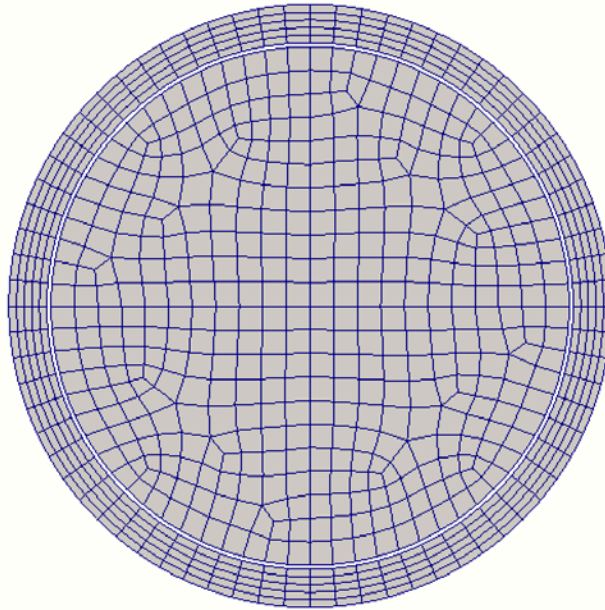


Figure 2-2: Azimuthal mesh used for BISON simulations.

The main feature of this mesh is the ability to split up each region into multiple sections. For this project the fuel rod and cladding was split up into 4 regions each allowing for azimuthal boundary and initially conditions to be specified separately for each region. This separation can be seen in Figure 2-3. Other variations to the boundaries and sections were made for each simulation. These changes will be highlighted in Chapter 3.

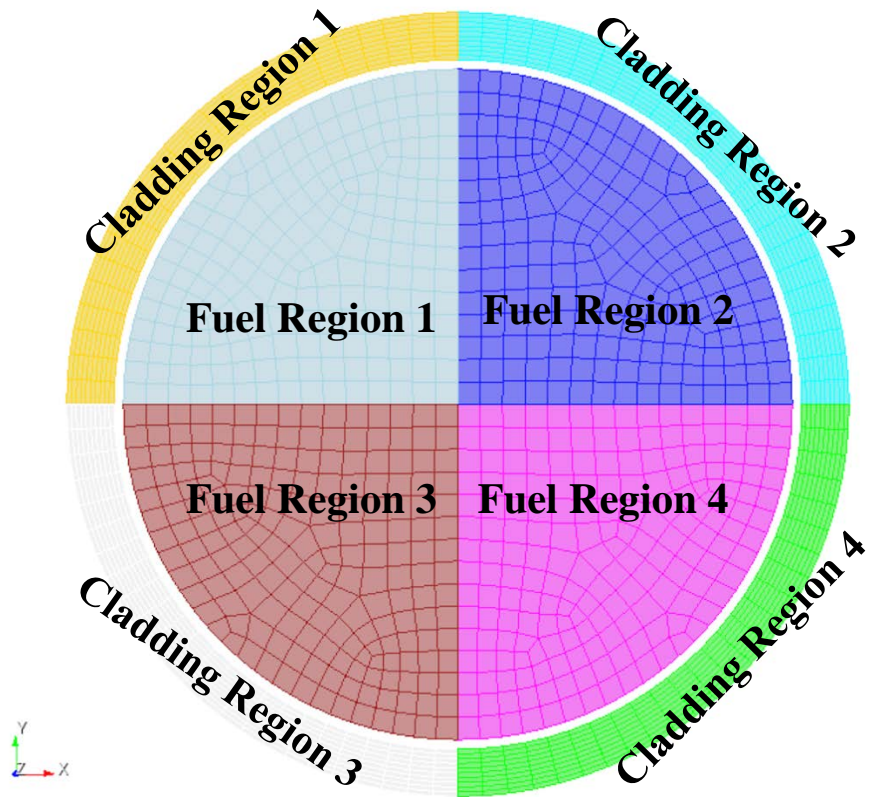


Figure 2-3: Azimuthal separation of the fuel rod and cladding.

Chapter 3 Simulation Results

This chapter shows the results of simulations of hydrogen heterogeneity in the azimuthal direction to ensure proper analysis of the hydrogen model. Reactor operating conditions are azimuthally heterogeneous. Therefore it is important to simulate these heterogeneous conditions to investigate the largest changes in hydrogen and hydride distributions.

As described in Chapter 1, hydrogen redistribution can be affected by various factors, the challenge of this work was to find the simulations that would cause the hydrogen within the cladding to redistribute under the most extreme situations. Only normal operating conditions have been considered in this study. With this in mind, three simulations were created to demonstrate extreme hydrogen redistribution: the introduction of a water rod near the fuel rod of interest, the introduction of a control rod near the fuel rod of interest, and the spallation of a portion of the oxide layer from the surface of the fuel cladding.

3.1 Water Rod located near the rod of interest

One possible effect of being near a water rod within the array is the production of an azimuthal temperature gradient, which may be significant depending on the nature of the fuel rods nearby. Hydrogen transport is related directly to temperature gradients as described in Chapter 1. By placing higher enriched fuel rods on the opposite region of a water rod, a large temperature gradient can be produced allowing for hydrogen transport due to the Soret Effect and Fick's law. To simulate this arrangement a 4x4 pin assembly, similar to that described in Chapter 2, is used with a water rod in location 6 and higher enriched fuel around the outer edge. This assembly geometry, with associated enrichments, is shown in Figure 3-1. The fuel rod of interest is depicted in Figure 3-1 with two *s. Figure 3-2 describes the initial temperature distributions for the four azimuthal sections produced by CTF. The parameters input for the CTF-DeCART model are found in Table 3-1.

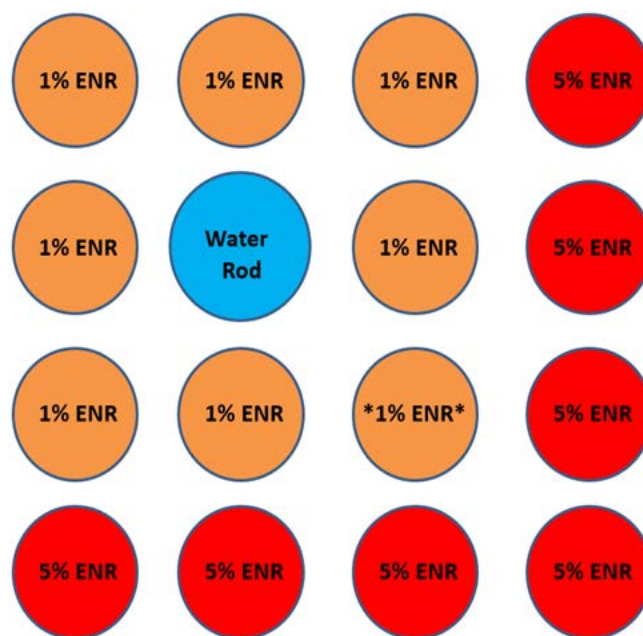


Figure 3-1: 4x4 pin water rod simulation schematic with associated enrichments.

305.1	305.0	304.8	304.5	303.7	310.7	334.2	341.5
1% Enr.		1% Enr.		1% Enr.		4% Enr.	
305.0	305.3	305.1	304.7	303.8	310.6	334.1	341.3
304.8	305.0	293.3	292.9	303.6	310.4	333.5	340.6
1% Enr.		Water Rod		1% Enr.		5% Enr.	
304.4	304.6	292.9	292.5	303.3	309.9	333.0	340.0
303.5	303.6	303.5	303.2	302.5	309.4	331.4	338.4
1% Enr.		1% Enr.		1% Enr.		5% Enr.	
310.7	310.5	310.4	310.0	309.3	312.2	334.3	337.4
333.9	333.8	333.2	332.7	331.2	334.1	332.4	335.6
5% Enr.		5% Enr.		5% Enr.		5% Enr.	
341.2	341.1	340.5	339.8	338.3	337.3	335.6	335.0

Figure 3-2: 4x4 pin water rod simulation schematic with beginning of cycle outer cladding temperatures at 0 burnup (°C).

Table 3-1: Parameters used in CTF and DeCART in the 4x4 water rod near the rod of interest simulation

Parameter	Value	Units
Reactor	PWR	
Layout	4 x 4	
Fuel	UO ₂	
High Enrichment	4.95	
Low Enrichment	1.00	
Fuel Density	10.4	g/cm ³
Percent Theoretical Density	0.95	
Burnable Poison	None	
Cladding	Zircaloy-4	
Cladding Density	6.55	g/cm ³
Coolant	H ₂ O	
Fill Gas	Helium	
Fill Gas Density	0.0002	g/cm ³
Fuel Pellet radius	4.095E-3	m
Cladding Inner Radius	4.18E-3	m
Cladding Outer Radius	4.75E-3	m
Cladding Thickness	5.70E-4	m
Pin Pitch	1.26E-2	m
Active Fuel Height	3.6576	m
Top Reflector Height	0.35512	m
Bottom Reflector Height	0.35512	m
Array Power	1.00	MW
Average Linear Heat Rate	18.5	kW/m
Core Pressure	15.5	MPa
Mass Flow Rate	4.86	Kg/s
Beginning of Cycle boron loading	1700	Ppm
Inlet Temperature	287	°C

A three-dimensional simulation was conducted in the CTF-DeCART coupling and a single slice of the fuel rod was used to generate the input files used within BISON as described in Section 2.1.3. In order to create a smooth and continuous cladding temperature, a parsed function was used that describes the cladding temperature as a function of time and space. The power history of the CTF-DeCART coupled simulation is shown in Figure 3-3. The power shown is the total linear heat rate in kW/m for all four fuel sections combined. Utilizing a total linear heat rate instead of four individual powers allows for a more simplified simulation.

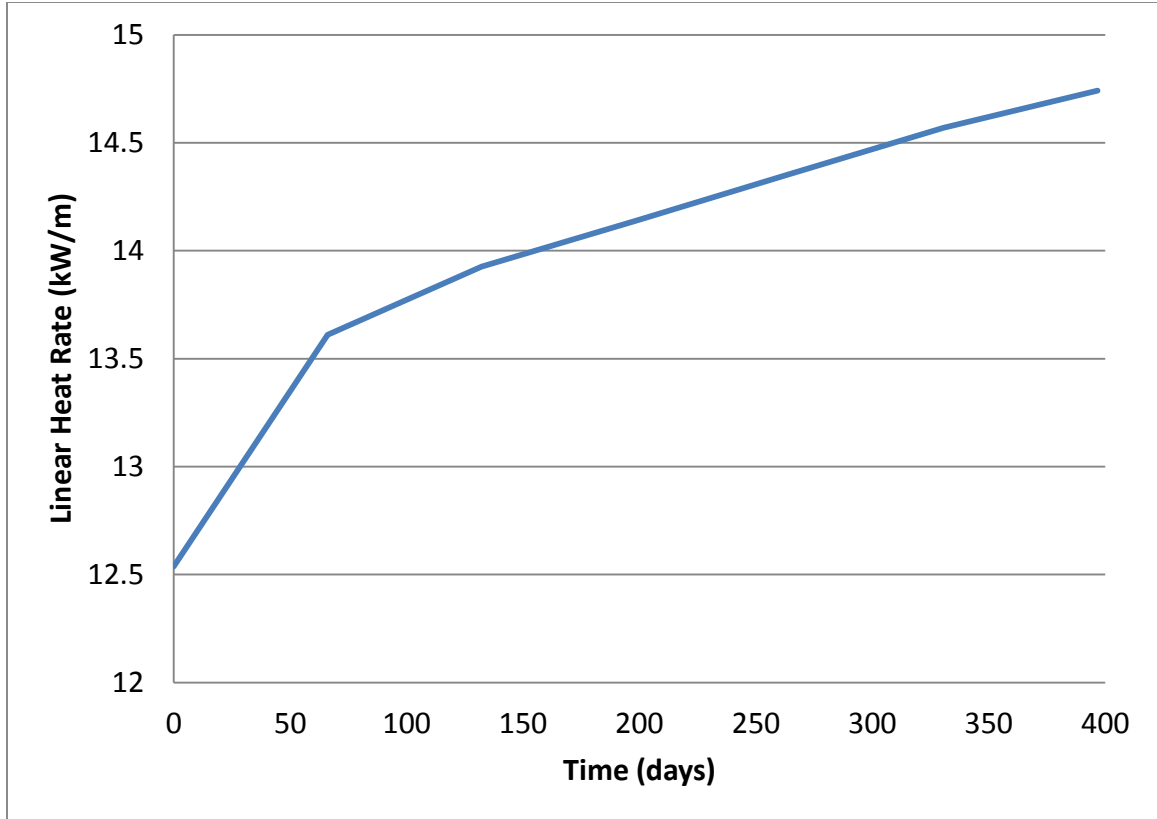


Figure 3-3: Total linear heat rate for the rod of interest.

Once this information is inputted, the simulation is run in BISON without any regards for the initial concentration of hydrogen to obtain the temperature distribution. Due to the interest in hydride formation around the rim, a scenario where precipitation occurs readily was created. First the outer cladding temperature on the hot side of the rod of interest is found using the previously mentioned method. Recalling the precipitation criterion found in Section 2.2.1, precipitation occurs when the concentration of hydrogen in solid solution is above the Terminal Solid Solubility limit (TSSp):

$$\text{if } C_{ss} > TSSp, \left\{ \begin{array}{l} \frac{dC_{ss}}{dt} = -\nabla \cdot J - \alpha^2 (C_{ss} - TSSp) \\ \frac{dC_p}{dt} = \alpha^2 (C_{ss} - TSSp) \end{array} \right\} \quad 2-13$$

$$TSSp_{\text{water_rod}} = 138745.0 \exp\left(-\frac{4145.72}{608 K}\right) = 151 \text{ wt. ppm}$$

Using this criterion, the initial hydrogen in solid solution concentration must exceed 151 wt. ppm to have precipitation in all azimuthal locations. Accordingly, for the purpose of this simulation, an initial homogeneous hydrogen in solid solution concentration of 200 wt. ppm was used for the cladding. The hydride concentration used was 0 wt. ppm everywhere.

Figure 3-4 through Figure 3-6 depict the cladding temperature distribution, hydrogen in solid solution distribution and hydrogen as hydrides distributions after 1 hour respectively. The first thing to note is the temperature gradient between the hot and cold sides of the cladding (bottom right and top left). The radial temperature gradient is approximately 15K, which agrees with analytical estimates. The azimuthal temperature gradient was approximately 10K. Note that in all of the following figures of temperature and hydrogen distributions, the numbers shown in the outside of the circle in approximately the 10 o'clock and 4 o'clock indicate the temperature (K) and hydrogen concentration (wt.ppm) for these locations. The hydrogen in solid solution concentration decreases from a homogeneous concentration of 200 wt. ppm to below 126 wt. ppm. This decrease in hydrogen in solid solution is expected because the hydrogen diffuses towards the outer rim where it precipitates as hydrides, see Figure 3-6. The concentration of hydrogen in hydrides increased from 0 wt.ppm to above 160 wt.ppm in the colder outer rim. The hydride concentration is also slightly higher on the cold side of the cladding. This is to be expected because the hydrogen in solid solution first diffuses to the colder region and the overall temperature gradient points towards the top left. It should be noted that the concentration of hydrogen in solid solution is lower in the colder region compared to the hot region. This is to be expected because the hydrogen did not have enough time to fully diffuse from the hot region and reach equilibrium. Had equilibrium been reached, the hydrogen in solid solution concentration should be higher in the cold region compared to the hot region.

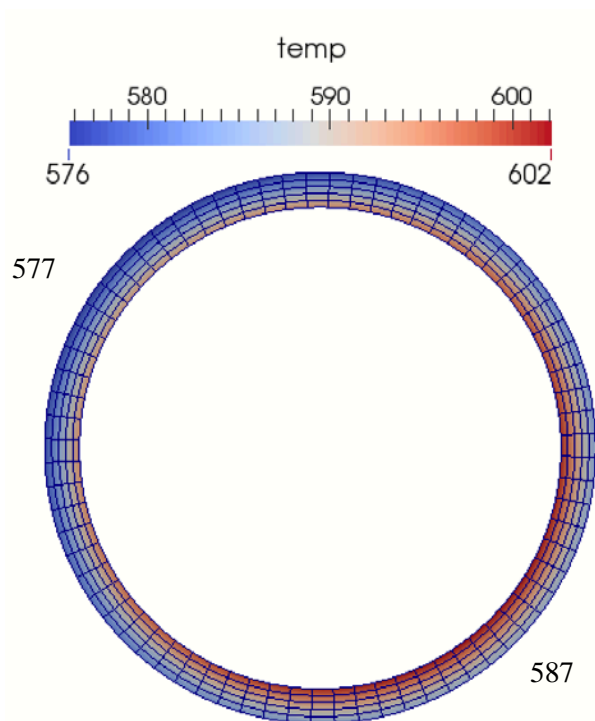


Figure 3-4: Azimuthal cladding temperature distribution (in degrees K) after 1 hour.

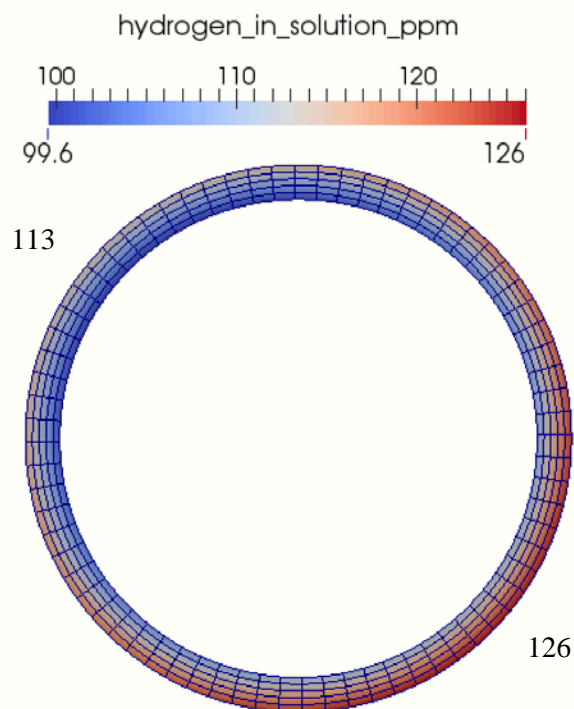


Figure 3-5: Azimuthal distribution of hydrogen in solid solution (wt.ppm) in the cladding after 1 hour.

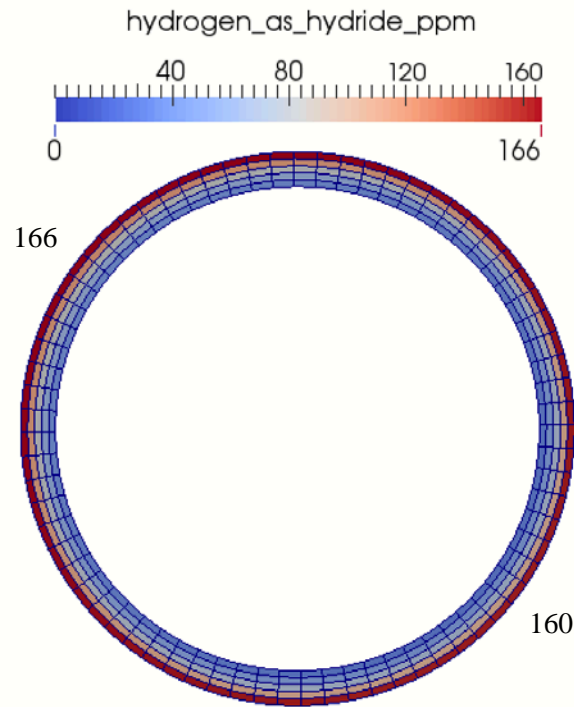


Figure 3-6: Azimuthal hydride distribution (wt.ppm) in the cladding after 1 hour.

Examining the evolution of the cladding temperature distributions after 1 week in the simulation in Figure 3-7 through Figure 3-9, it can be seen that the temperature gradient between the hot and cold regions is almost always roughly 10°C with only small changes to the outer cladding temperatures. This means that hydrogen in solid solution and the hydrides concentrations are exposed to a nearly constant temperature gradient. This allows for hydrogen in solid solution to diffuse towards an equilibrium state, while hydrogen precipitates as hydrides until it reaches a predetermined cap of 1000 wt.ppm as described in [21].

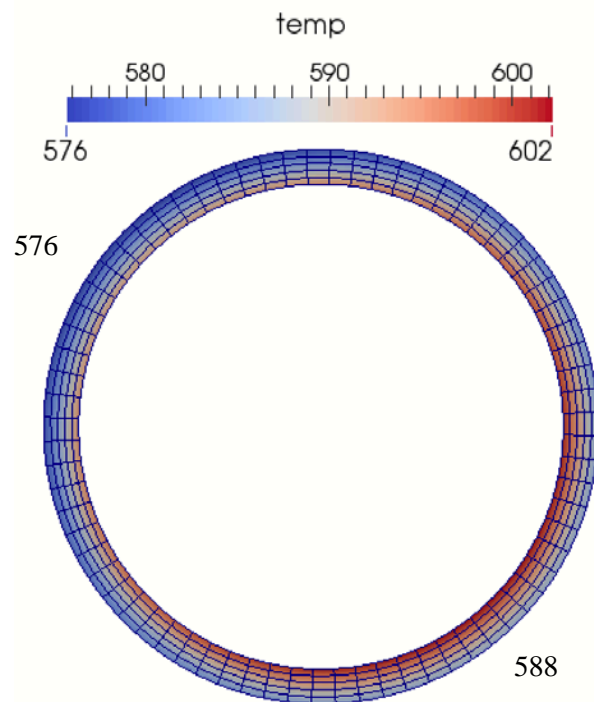


Figure 3-7: Azimuthal cladding temperature distribution (in degrees K) after 1 day

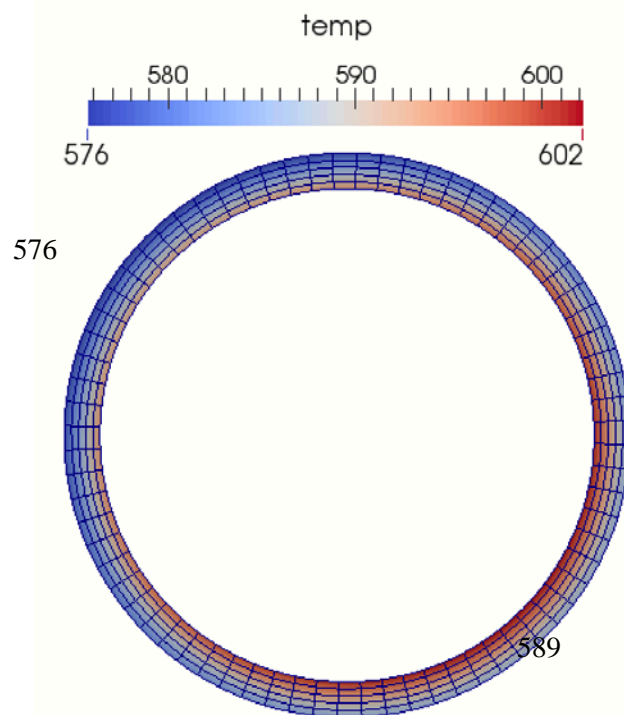


Figure 3-8: Azimuthal cladding temperature distribution (in degrees K) after 7 days.

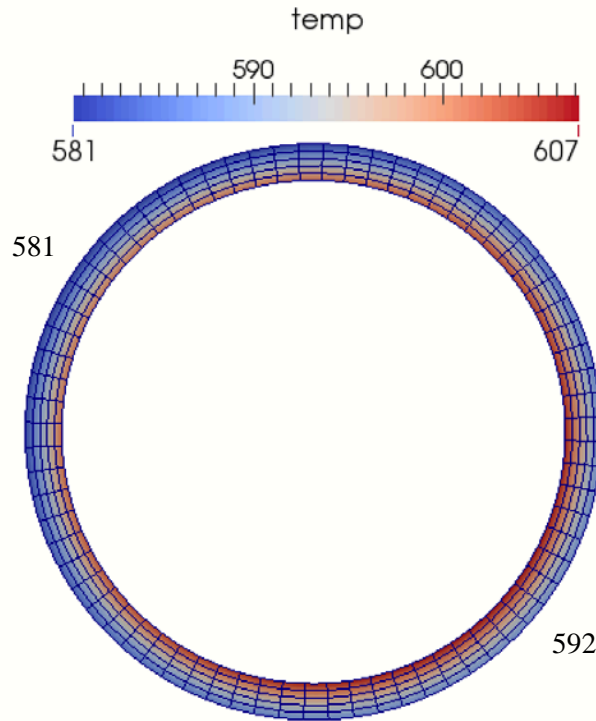


Figure 3-9: Azimuthal cladding temperature distribution (in degrees K) after 1 year.

Figure 3-10 and Figure 3-11 shows the hydrogen in solid solution and hydrogen as hydrides distributions after 1 day. The hydrogen in solid solution concentration continues to decrease and still has not reached equilibrium. The hydrogen continues to precipitate into hydrides to form a hydride rim with the more favorable location for precipitation being in the colder region. The concentration of hydrogen in hydrides will not decrease unless the dissolution criterion is met, shown again below.

$$\text{if } TSSd \geq C_{ss} \text{ and } C_p > 0 \text{ and } \nabla J > 0$$

$$\text{then } \left\{ \begin{array}{l} \frac{dC_{ss}}{dt} = -\nabla \cdot J + \beta^2(TSSd - C_{ss}) \\ \frac{dC_p}{dt} = -\beta^2(TSSd - C_{ss}) \end{array} \right\} \quad 3-1$$

This would mean that dissolution would occur when the hydrogen in solid solution falls below the TSSd which occurs at roughly 86 wt.ppm as shown in the calculation below.

$$TSSd_{water_rod} = 106446.7 \exp\left(-\frac{4328.67}{608 K}\right) = 86 \text{ wt. ppm}$$

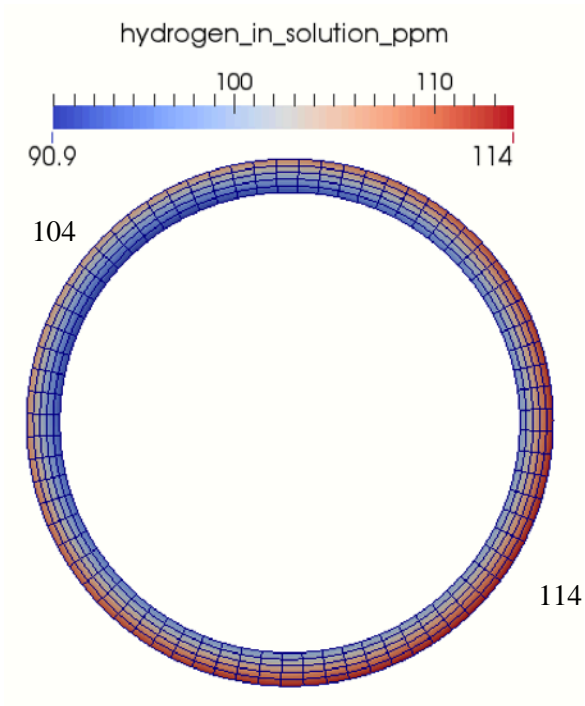


Figure 3-10: Azimuthal distribution of hydrogen in solid solution (wt.ppm) in the cladding after 1 day.

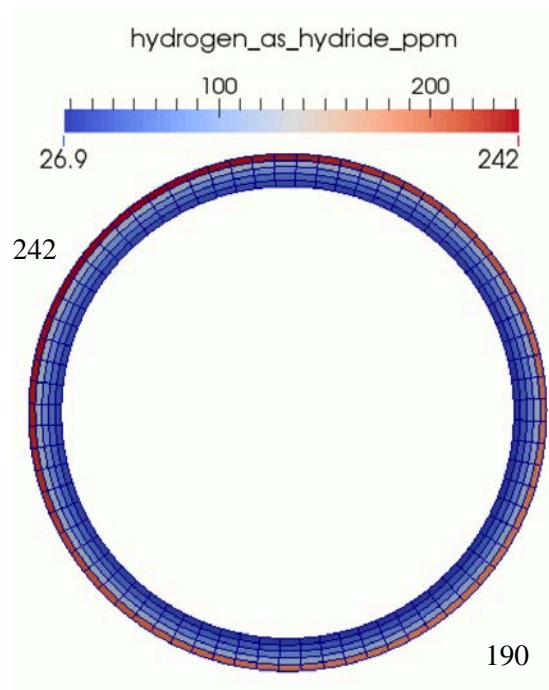


Figure 3-11: Azimuthal hydride distribution (wt.ppm) in the cladding after 1 day.

Figure 3-12 shows the hydrogen in solid solution distribution after about 7 days. The hydrogen has already had enough time to diffuse to colder regions as shown by the higher concentration compared to the hot region. Figure 3-14 is the hydrogen in solid solution distribution after about 1 year. When compared to Figure 3-12 it becomes clear that the hydrogen in solid solution has nearly reached an equilibrium concentration in the two extremes. Some small amount of diffusion continues as the remaining hydrogen in solid solution continues to diffuse from one extreme to the other. This can be seen by the change in minimum concentration from around 87 wt.ppm to about 85 wt.ppm which is only a slight change. Figure 3-13 is the hydrogen in hydrides distribution after about 7 days. The cold region contains more than double the concentration of the hot region indicating the process of forming the hydride rim. The large step between the outer node and the next to last node is primarily numerical. The simulation contains a single point that the hydrides would most favorably precipitate. Realistically a smoother hydride rim would be observed. Figure 3-15 shows the hydrogen as hydrides distribution after 1 year. When compared to hydride distribution in Figure 3-13, the hot region reached an equilibrium concentration of 190 wt.ppm. This is likely because all of the hydrogen in solid solution available for precipitating has already diffused to a different region. The hydride concentration in the cold region has reached the concentration cap of 1000 wt.ppm. This acts as a locked mesh cell making the two mesh cells surrounding it the next favorable precipitation locations. This is the reason for the hydrogen as hydride precipitating in specific locations rather than as a smoother hydride rim. Figure 3-13 and Figure 3-15 show an increasing amount of hydrogen concentration in the colder region of the rod. After 1 year, Figure 3-15, the total amount has reached the limit of 1000 wt.ppm and can be considered as the best simulation we now have of a hydride rim. Note that the hydrogen distributions shown are at temperature. As the rod cools, before examination at room temperature the hydrogen in solid solution precipitates creating additional hydrides.

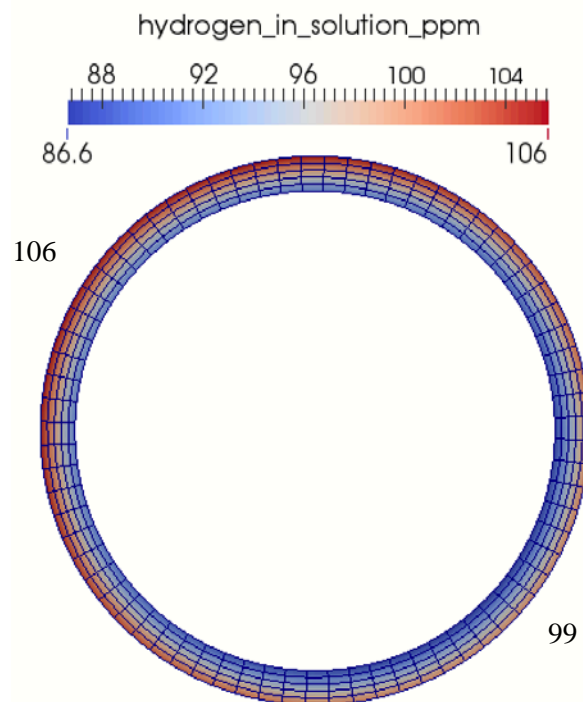


Figure 3-12: Azimuthal distribution of hydrogen in solid solution (wt.ppm) in the cladding after 7 days.

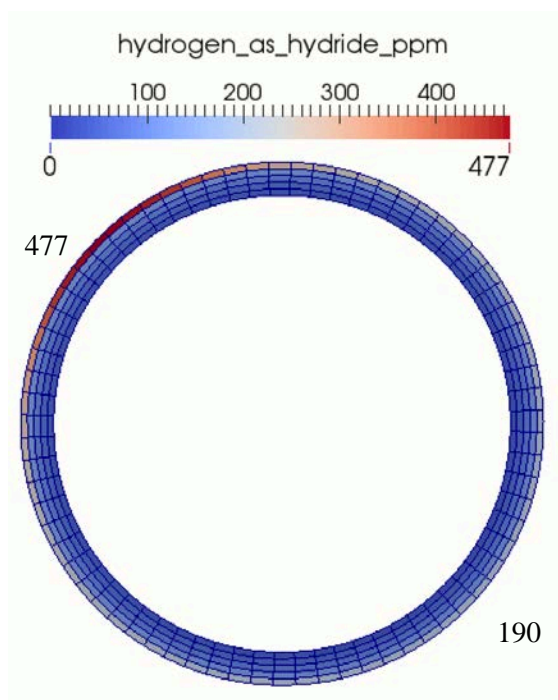


Figure 3-13: Azimuthal hydride distribution (wt.ppm) in the cladding after 7 days.

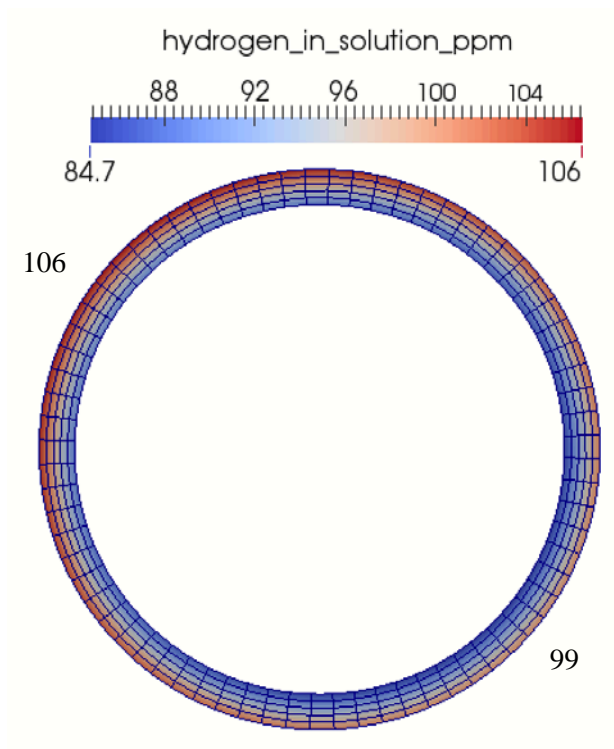


Figure 3-14: Azimuthal distribution of hydrogen in solid solution (wt.ppm) in the cladding after 1 year.

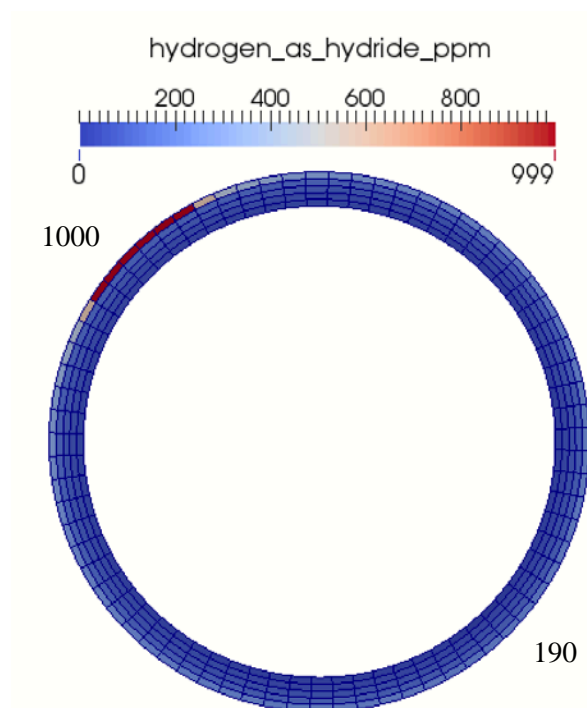


Figure 3-15: Azimuthal hydride distribution (wt.ppm) in the cladding after 1 year.

3.2 Control Rod located near the rod of interest

The next simulation conducted in this project is the partial insertion of a control rod near the rod of interest. When a control rod is inserted into a reactor the power near that location decreases proportional to the amount inserted. This simulation was conducted to observe the effects of an azimuthal power gradient on hydrogen and hydride distributions. A 4x4 pin assembly, similar to that of the previous simulation in Section 3.1, was used with a control rod located in location 6 instead of a water rod. The assembly geometry can be seen in Figure 3-16 along with the associated enrichments of each pin and in Figure 3-17 with the associated azimuthal temperatures at the beginning of cycle. The parameters input for the CTF-DeCART model are the same as those found in the previous simulation and found in Table 3-1. Note that the rod of interest is surrounded by fresh rods on one side while having a control rod on the other, which should cause a high azimuthal temperature gradient.

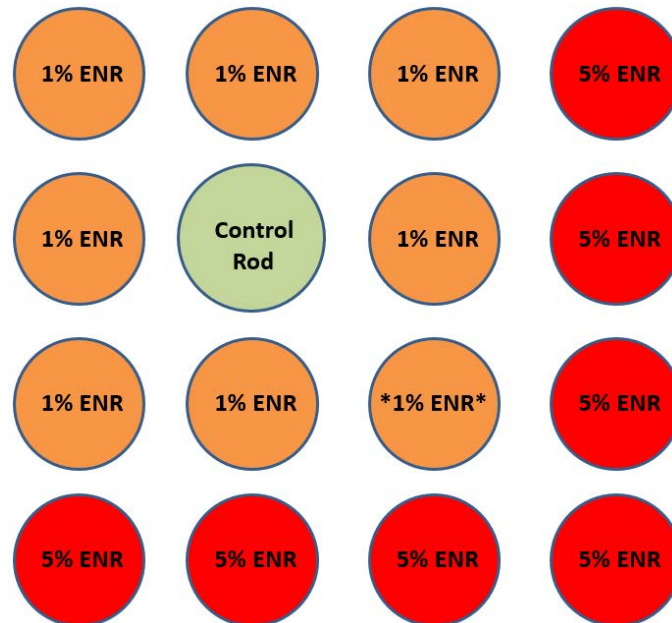


Figure 3-16: 4x4 pin assembly with control rod schematic with associated enrichments.

308.6	308.2	307.5	307.9	309.3	319.1	337.6	345.9
1% Enr.		1% Enr.		1% Enr.		5% Enr.	
308.2	308.1	307.4	307.8	309.3	318.9	337.4	345.9
307.5	307.3	296.9	297.3	308.6	318.3	337.3	345.8
1% Enr.		Control Rod		1% Enr.		5% Enr.	
307.7	307.7	297.3	297.7	308.9	318.5	337.5	345.9
309.0	309.0	308.3	308.7	310.0	319.5	337.9	346.0
1% Enr.		1% Enr.		1% Enr.		5% Enr.	
318.8	318.7	318.1	318.4	319.6	324.6	342.9	346.1
336.7	336.5	336.5	336.8	337.5	342.6	342.9	346.1
5% Enr.		5% Enr.		5% Enr.		5% Enr.	
345.6	345.6	345.6	345.7	345.9	346.0	346.1	346.1

Figure 3-17: 4x4 pin water rod simulation schematic with beginning of cycle outer cladding temperatures at 0 burnup ($^{\circ}\text{C}$).

A three-dimensional simulation was conducted in the CTF-DeCART coupling and a single slice of the fuel rod was used to generate the input files used within BISON, as described in Section 2.1.3. In order to create a smooth and continuous cladding temperature, a parsed function was used that describes the cladding temperature as a function of time and space in the same manner as the previous simulation. The simulation was run for one burnup step, approximately 66 days, using the power history seen in Figure 3-18.

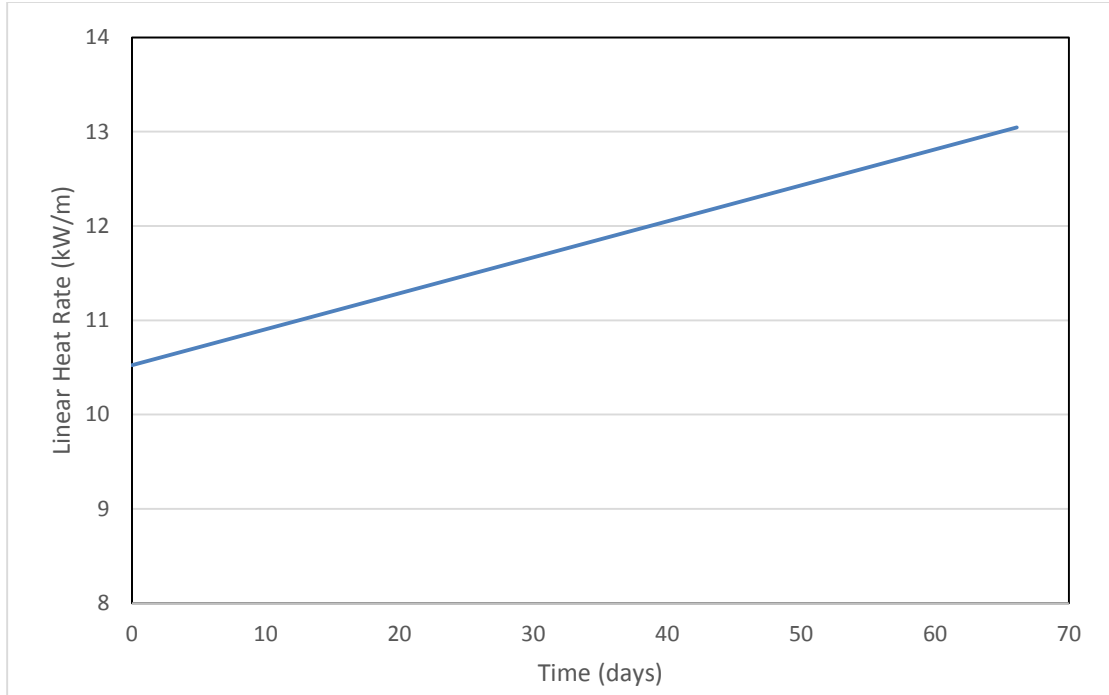


Figure 3-18: Total linear heat rate for the rod of interest.

Similar to the previous simulation, the simulation first run without regard for the initial hydrogen in solid solution and hydrogen as hydrides concentrations. The outer cladding temperature in the hot region is then used to calculate the initial hydrogen in solid solution by ensuring the is remains above the TSSp. This forces hydrides to form everywhere on the outer cladding surface. To have hydride precipitation the concentration needed to exceed 155 wt.ppm as shown below.

$$TSSp_{control_rod} = 138745.0 \exp\left(-\frac{4145.72}{610 K}\right) = 155 \text{ wt. ppm}$$

An initial hydrogen in solid solution concentration of 200 wt.ppm and initial hydrogen as hydrides concentration of 0 wt.ppm were chosen. Figure 3-19 through Figure 3-21 depict the cladding temperature distribution, hydrogen in solid solution distribution and hydrogen as hydrides distributions after 1 day, respectively. The cold region is located in the top left and the hot region is the bottom right, similar to that of the water rod simulation. The hydrogen in solid solution concentration decreases from a homogeneous concentration of 200 wt. ppm to below 123

wt. ppm on the outer cladding surface. This decrease in hydrogen in solid solution is expected because the hydrogen diffuses towards the outer rim where it precipitates as hydrides due to the high hydrogen in solid solution concentration. The concentration of hydrogen as hydrides increased from 0 wt.ppm to above 169 wt.ppm with the more favorable location for precipitation being at the cold region again. The hydrogen in solid solution concentration is lower in the cold region compared to the hot region. This means that equilibrium has not been reached and during the initial part of the simulation hydrogen will diffuse to the cold region.

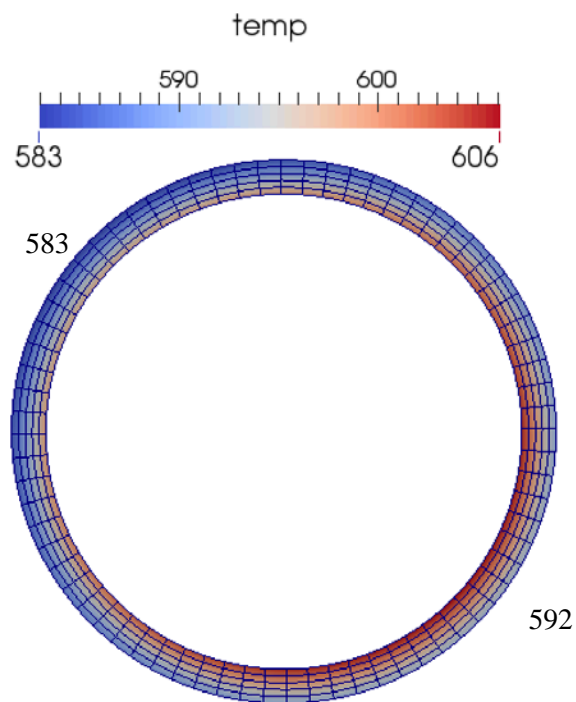


Figure 3-19: Azimuthal cladding temperature distribution (in degrees K) after 1 day.

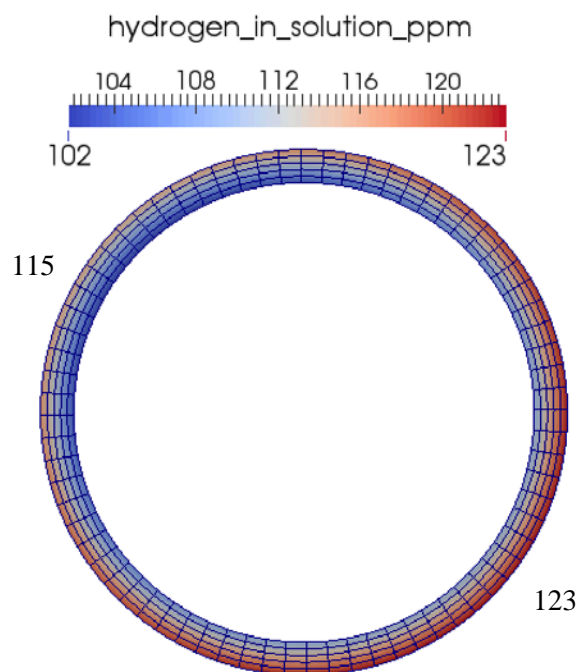


Figure 3-20: Azimuthal hydrogen in solid solution distribution (wt.ppm) in the cladding after 1 day.

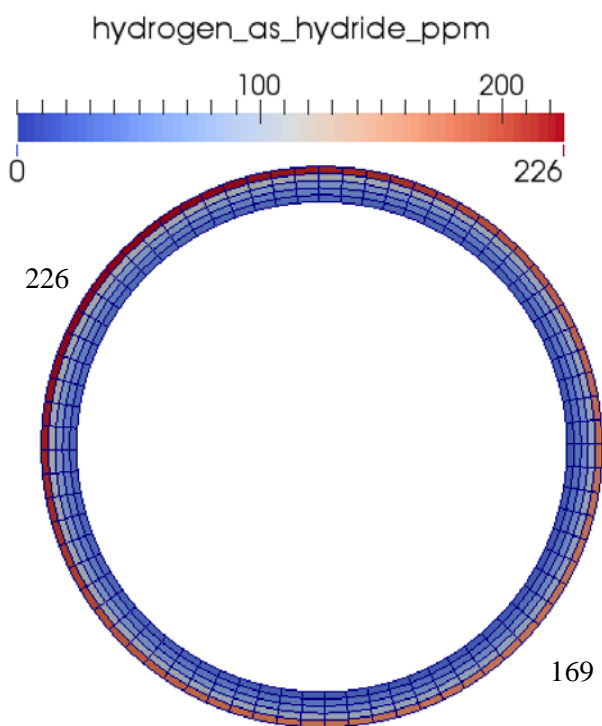


Figure 3-21: Azimuthal hydride distribution (wt.ppm) in the cladding after 1 day.

When comparing the cladding temperature distributions for the remainder of the simulation (Figure 3-22 through Figure 3-24), there is a slight increase in outer cladding temperature. The temperature gradient between the hot region and the cold region is nearly constant with the average temperature difference being about 9 degrees. Given enough time, the hydrogen in solid solution should reach equilibrium at the hot and cold regions while precipitating in the favored locations until the concentration at these locations reaches the cap of 1000 wt.ppm.

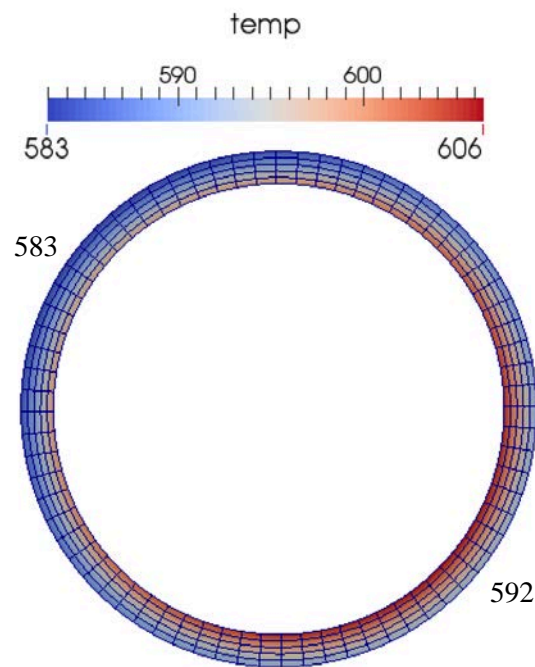


Figure 3-22: Azimuthal cladding temperature distribution (in degrees K) after 1 week.

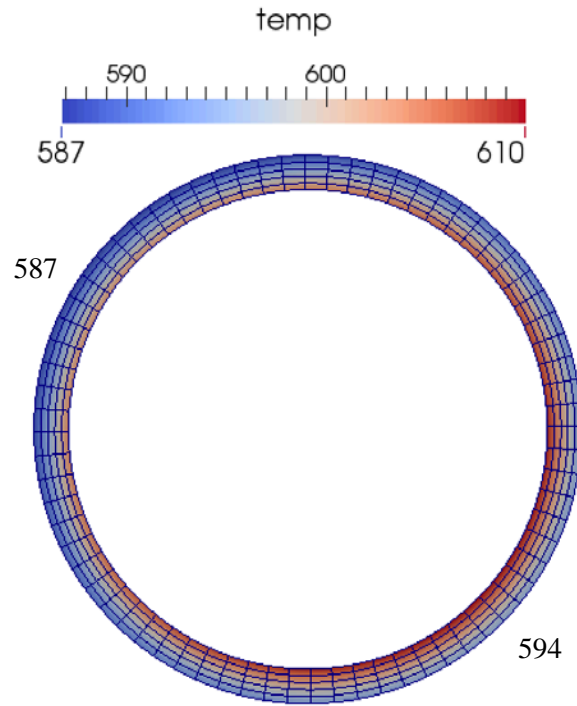


Figure 3-23: Azimuthal cladding temperature distribution (in degrees K) after 33 days.

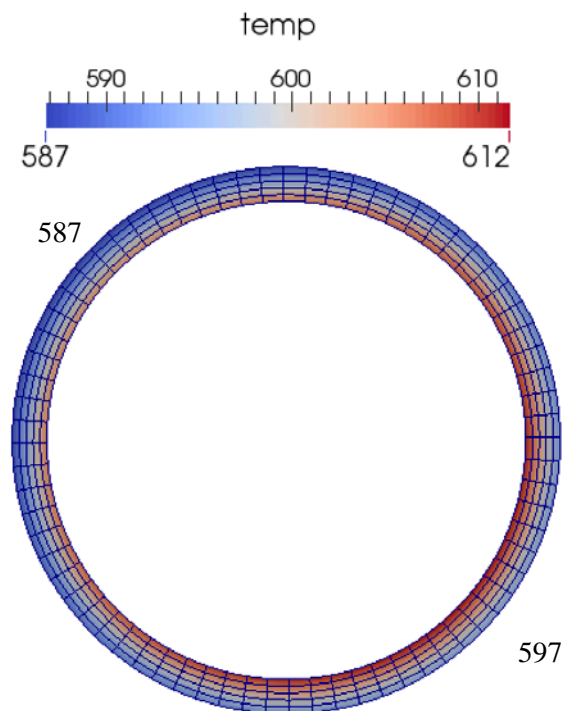


Figure 3-24: Azimuthal cladding temperature distribution (in degrees K) after 66 days.

Figure 3-25 and Figure 3-26 show the distribution of hydrogen in solid solution and hydrides distributions after 7 days. The hydrogen in solid solution concentration diffused to the colder region and continued to drop to below 115 wt.ppm as precipitation occurred. Precipitation continues in to form a hydride rim in Figure 3-26. The high concentration in the cold region compared to the hot region is similar to the water rod simulation. In order for the hydride concentration to dissolve, the hydrogen in solid solution would need to fall below the TSSd which occurs at roughly 88 wt.ppm as shown in the calculation below. This does not occur at any point in this simulation.

$$TSSd_{control_rod} = 106446.7 \exp\left(-\frac{4328.67}{610 K}\right) = 88 \text{ wt. ppm}$$

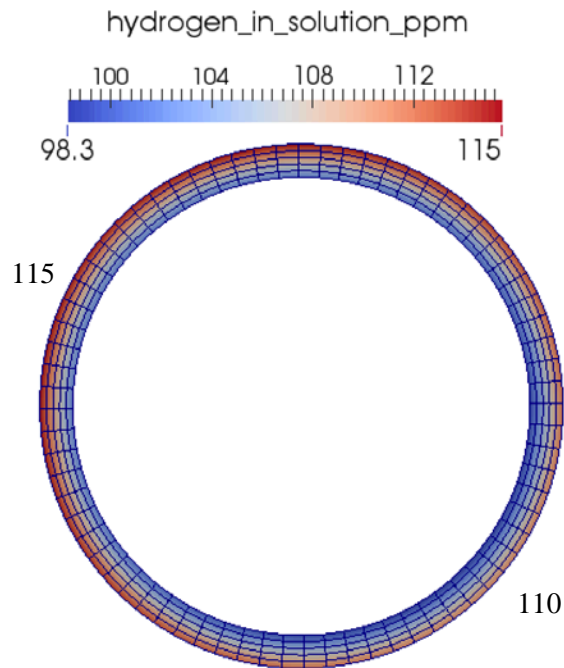


Figure 3-25: Azimuthal hydrogen in solid solution distribution (wt.ppm) in the cladding after 7 days.

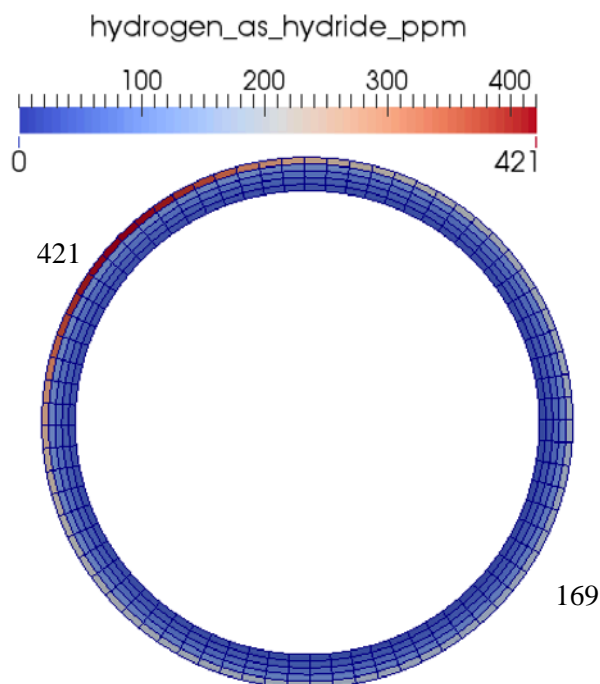


Figure 3-26: Azimuthal hydride distribution (wt.ppm) in the cladding after 7 days.

Figure 3-27 shows the hydrogen in solid solution distribution after the simulation was run for 33 days. Compared to the hydrogen in solution distribution after 66 days in Figure 3-29, there is a small amount of hydrogen diffusion from the hot region to the cold region. This is to be expected, because there is only a small increase in the outer cladding temperature between 33 and 66 days. Figure 3-28 shows the hydride distribution after 33 days. The hydride concentration nearly doubles from 1 day to 33 days after as seen in Figure 3-30. The high concentration of hydrides can be seen here as well. The highest value of the hydrogen concentration in the rim is artificially set at 1000 wt.ppm and reaches that value quickly. The higher concentration of hydrogen in solid solution serving as a source for that precipitation.

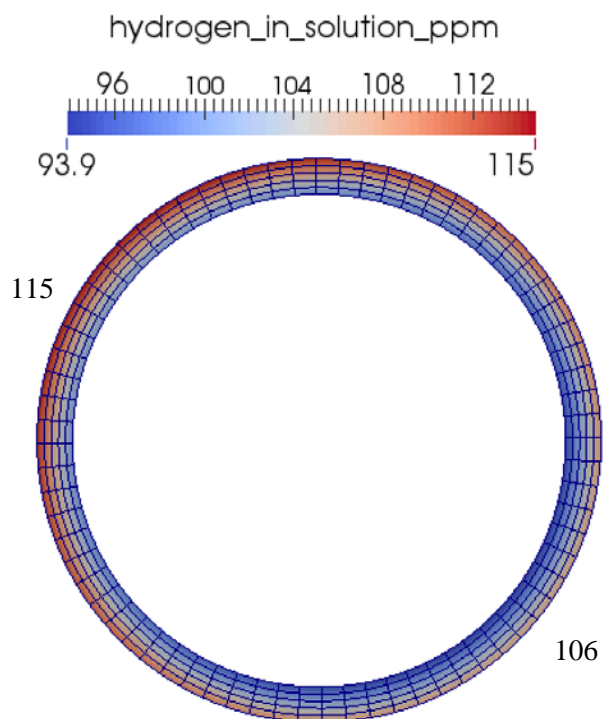


Figure 3-27: Azimuthal hydrogen in solid solution distribution (wt.ppm) in the cladding after 33 days.

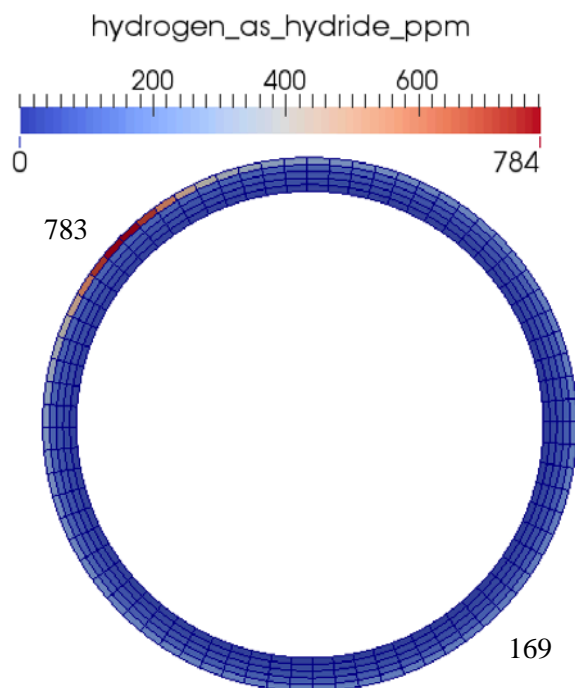


Figure 3-28: Azimuthal hydride distribution (wt.ppm) in the cladding after 33 days.

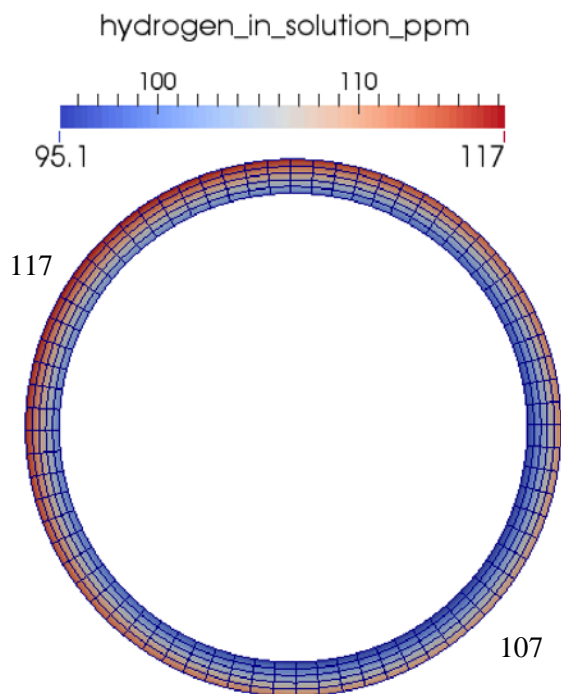


Figure 3-29: Azimuthal hydrogen in solid solution distribution (wt.ppm) in the cladding after 66 days.

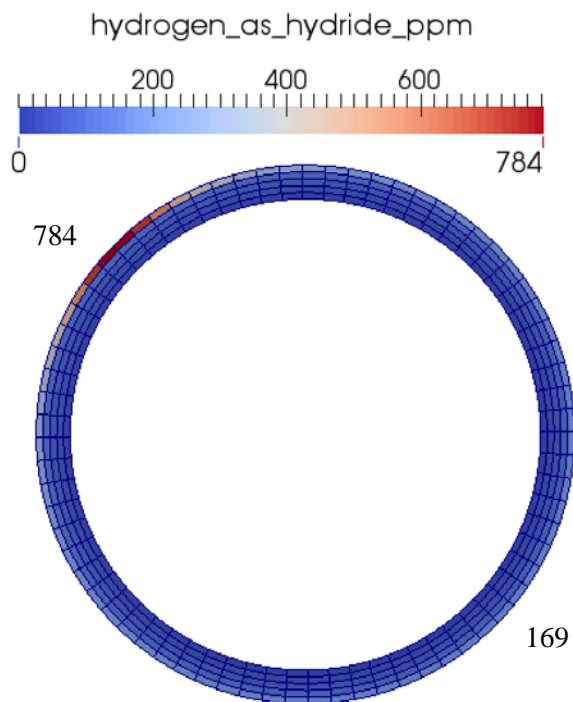


Figure 3-30: Azimuthal hydride distribution (wt.ppm) in the cladding after 66 days.

The results of this simulation again indicate a strong tendency of the hydrogen to concentrate on one azimuthal location of the cladding.

3.3 Spallation of Zirconium Oxide

As the oxide layer thickness increases above 60-80 microns, there is a chance that a portion this layer may break off or spall. When this happens, the new surface is directly exposed to the water coolant creating a local temperature gradient. Often a hydride blister is observed can be created at that location because the hydrogen in solid solution first diffuses towards this region and precipitates there. A simulation was created to mimic this phenomenon. CTF and DeCART are not able to easily simulate the spallation of zirconium oxide. For this reason the entire simulation was performed using BISON.

A few changes to the mesh boundaries and input deck were made in order to create this distribution. Firstly, one of the four cladding regions needed to be treated as an individual area with separate boundary conditions. To model the missing oxide, a thermal resistance calculation was performed to calculate the equivalent thermal conductivity needed. Figure 3-31 shows the schematic of the thermal resistance.

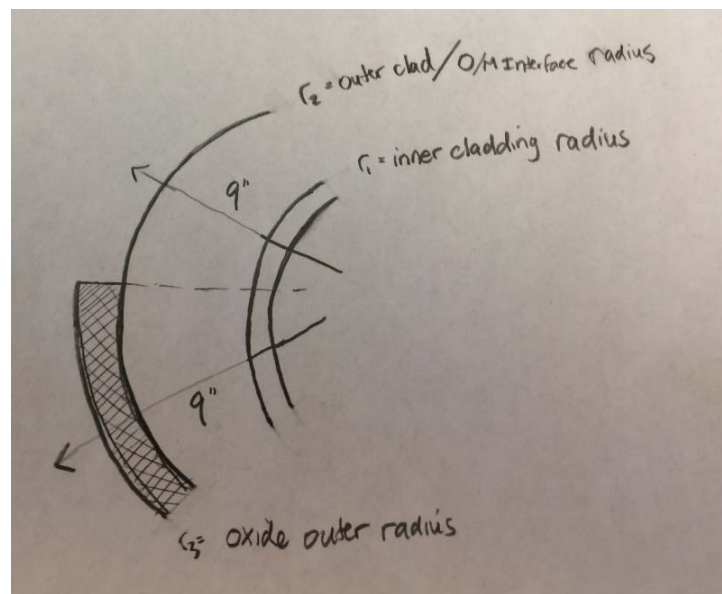


Figure 3-31: Schematic of thermal resistance calculation

Where,

r_1 is the inner cladding radius, r_2 is the oxide-cladding interface radius, r_3 is the outer cladding radius, k_1 is the thermal conductivity of zirconium 16 W/mK, k_2 is the thermal conductivity of the oxide 1.6 W/mK and k_{equi} is the equivalent thermal conductivity of cladding with oxide layer, given by:

$$k_{equi} = \frac{\ln\left(\frac{r_3}{r_1}\right)}{\frac{\ln\left(\frac{r_2}{r_1}\right)}{k_1} + \frac{\ln\left(\frac{r_3}{r_2}\right)}{k_2}} \quad 3-2$$

The inner cladding radius is 4.16 mm, the outer cladding radius is 4.76 mm and assuming an oxide thickness of 100 μm , the following equivalent thermal conductivity is calculated.

$$k_{equi} = \frac{\ln\left(\frac{4.77}{4.16}\right)}{\frac{\ln\left(\frac{4.76}{4.16}\right)}{16} + \frac{\ln\left(\frac{4.77}{4.76}\right)}{1.6}} = 14.0 \frac{W}{mK} \quad 3-3$$

The BISON input deck was updated to include this thermal conductivity for the 3 regions while the spalled region used a thermal conductivity of 16 W/mK (same as Zr). Rather than using a parsed function formulated using information from CTF, BISON internally calculated the outer cladding temperature distribution. A uniform power history of 25 kW/m was used for this simulation. Similar to the previous simulations, the initial hydrogen in solid solution concentration was determined by first running the simulation then making sure the initial concentration was above the TSSp to meet the precipitation criterion.

$$TSSp_{spall_oxide} = 138745.0 \exp\left(-\frac{4145.72}{641 K}\right) = 215 \text{ wt. ppm}$$

This means that the initial hydrogen in solid solution concentration should be above 215 wt.ppm so that an initial homogeneous concentration of 300 wt.ppm was assumed. The initial hydrogen as

hydrides was 0 wt. ppm. In order for dissolution of hydrides to occur, the hydrogen as hydrides concentration needs to fall below 124 wt.ppm as shown in the calculation below.

$$TSSd_{Spall\ Oxide} = 106446.7 \exp\left(-\frac{4328.67}{641\ K}\right) = 124\ wt.ppm$$

Figure 3-32 though Figure 3-34 depict the cladding temperature distribution, hydrogen in solid solution distribution and hydrogen as hydrides distribution after 1 day. Because the cold region is simulated using an equivalent thermal conductivity, the temperature gradient between the hot region is not as apparent. There is a larger gradient at the boundary between regions which will play an important role later in the simulation.

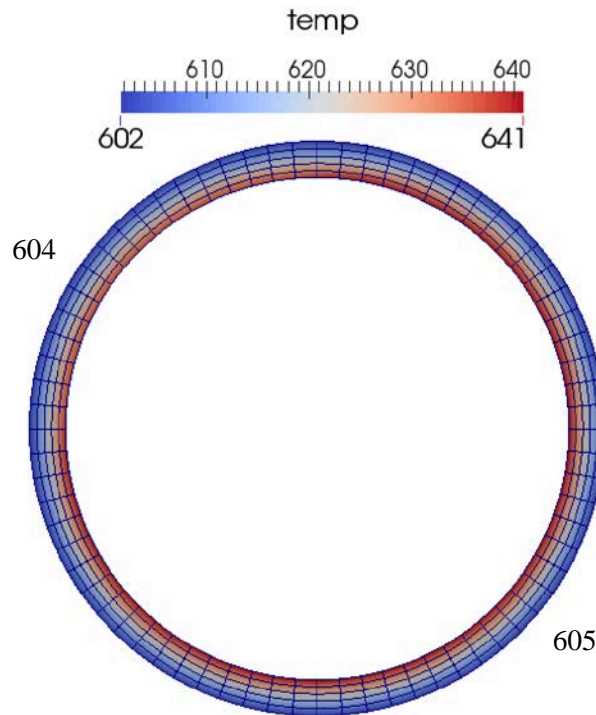


Figure 3-32: Azimuthal cladding temperature distribution after 1 day in Kelvin

The hydrogen in solid solution concentrations shown in Figure 3-33 are expected, given the previous argument about using an equivalent thermal conductivity. There is a higher concentration of hydrogen in solid solution in the colder region compared to the hot region. Note that after 1 day the hydrogen concentration in solid solution dropped to nearly half of the initial

300 wt.ppm concentration. The hydride distribution in Figure 3-34 differs from previous simulations. The hydrides begin forming at the interface between the spalled region and non-spalled region. The entire spalled region should have developed a more significant increase in hydride concentration. Instead the temperature gradient at the interfaces acts almost like the entire spalled region. This is because the hydrogen in solid solution that diffuses into the colder region immediately precipitates at the interface rather than potentially diffusing further into the spalled region. The hydride concentration then continues to increase until the concentration cap is reached and a new favorable precipitation region is made.

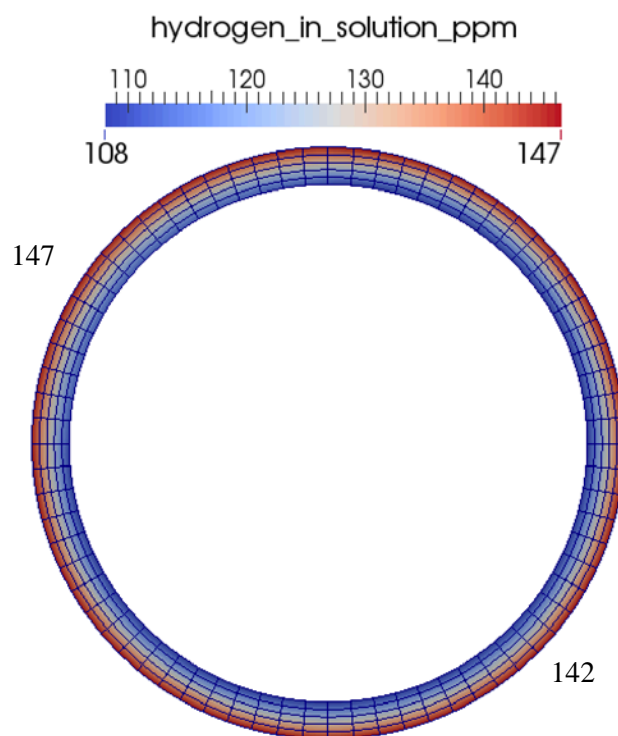


Figure 3-33: Azimuthal hydrogen in solid solution distribution (wt.ppm) in the cladding after 1 day.

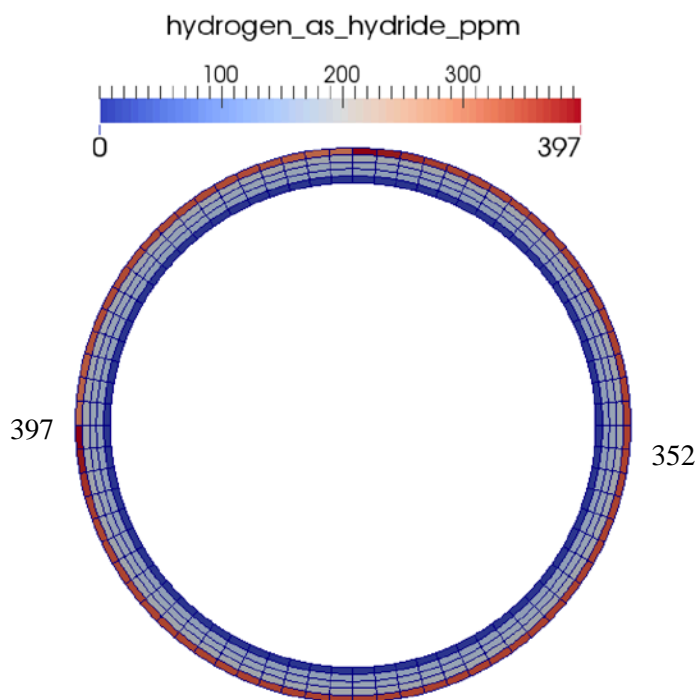


Figure 3-34: Azimuthal hydride distribution (wt.ppm) in the cladding after 1 day.

The cladding temperature distribution found in Figure 3-32 is constant throughout the simulation as seen in Figure 3-36 after 1 year.

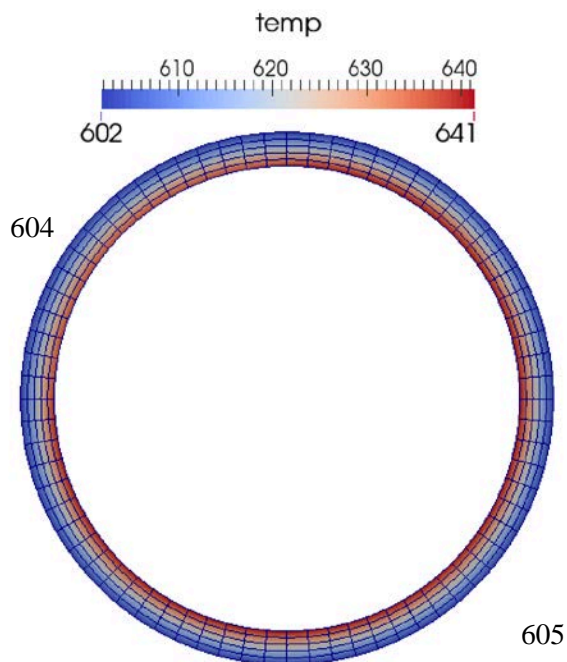


Figure 3-35: Azimuthal cladding temperature distribution (in degrees K) after 1 year.

Figure 3-36 shows the hydrogen in solid solution distribution after 30 days which has not changed likely due to the constant temperature distribution and reaching equilibrium state i.e any diffused hydrogen in solid solution precipitates at one of the favored locations instead of remaining in solid solution. Figure 3-37 shows the hydrogen as hydrides distribution after 30 days. The favored precipitation locations nearly reached the concentration limit and will then create more favored locations. Most of the hydrides that would precipitate in the spalled region all diffuses to the boundary and precipitates there. Figure 3-38 shows the hydrogen in solid solution distribution after 1 year which has not changed significantly. Figure 3-39 is the hydrogen as hydrides distribution after 1 year. The hydride concentration has already reached the cap in a few cells and cannot diffuse through filled locations. This means that the hydrogen in solid solution would need to go around the capped cell which can be seen by the concentration being higher in the spalled region compared to the hotter region.

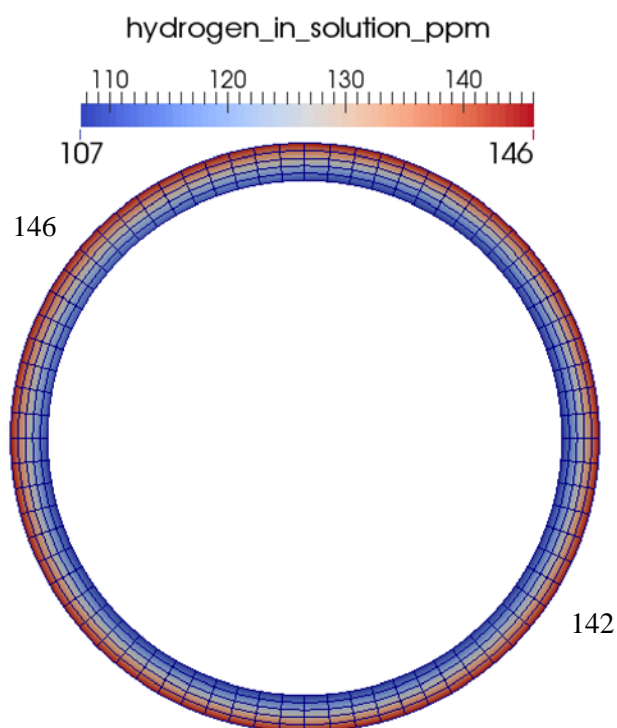


Figure 3-36: Azimuthal hydrogen in solid solution distribution (wt.ppm) in the cladding after 30 days.

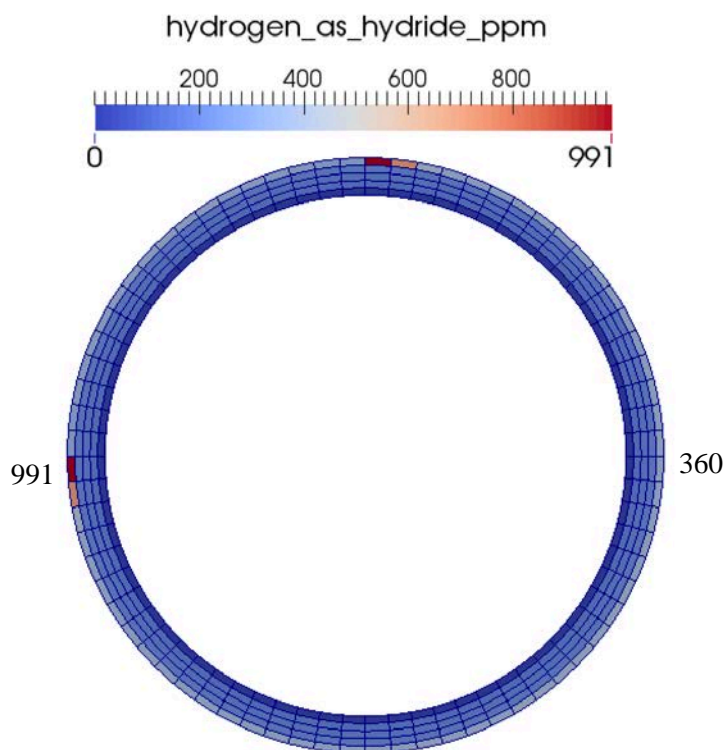


Figure 3-37: Azimuthal hydride distribution (wt.ppm) in the cladding after 30 days.

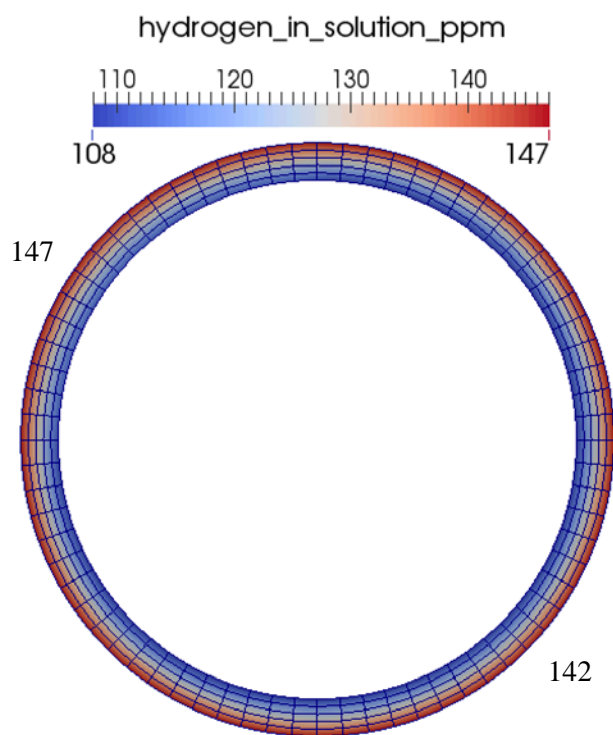


Figure 3-38: Azimuthal hydrogen in solid solution distribution (wt.ppm) in the cladding after 1 year.

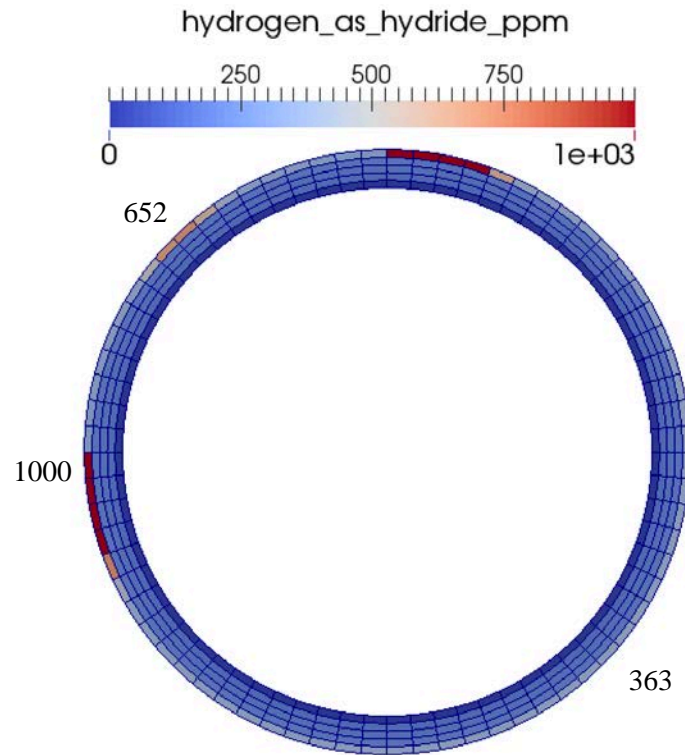


Figure 3-39: Azimuthal hydrogen as hydrides distribution (wt.ppm) in the cladding after 1 year.

Chapter 4 Conclusions and Future Work

The azimuthal dependence of hydrogen and hydride distributions was modeled using BISON fuel performance code coupled indirectly with the Penn State maintained thermal-hydraulics code, COBRA-TF, and the neutronics code, DeCART. Three simulations were conducted to obtain the temperature, hydrogen and hydride distributions under conditions where large variations in azimuthal hydrogen distribution should be expected.

One of the simulations included a water rod near the rod of interest. In this simulation, the water rod created an azimuthal temperature gradient for hydrogen transport and precipitation to occur. The hydrogen in solid solution diffused to the colder region, as expected, and precipitated as hydrides on the outer rim of the cladding. We believe this hydride rim mimics real cases. After 1 year, hydride concentration reached an artificial concentration limit of about 1000 wt.ppm.

The next simulation was a control rod located near the rod of interest. By placing a control rod on one side and high enriched fuel on the other side, an azimuthal temperature gradient was created for hydrogen transport and precipitation to occur. The simulation was run for one burnup step (66 days). Within this burnup step, the hydrogen in solid solution diffused to the outer rim and precipitated as hydrides very quickly. The hydride rim did not contain as many hydrides as the water rod near the rod of interest simulation, but the concentration was still a significant amount.

Finally, the last simulation included a portion of the cladding breaking off from the cladding. This simulation did not produce realistic results, but pointed the way to performing a correct simulation by providing a smoother transition in temperature profiles between interfaces.

A common tendency for all of the above simulations was that hydrogen diffused to the cold region and precipitated as hydrides there, as expected. The coupled codes can be used now

more extensively to investigate the range of hydrogen concentrations expected in nuclear fuel cladding.

In the future, the hydrogen model can be improved by studying and including the effects of stresses on hydrogen transport and precipitation mechanisms. Currently, work is being done on directly coupling BISON to the thermal-hydraulics code (CTF) and the neutronics code (MPACT). With this coupling, results should improve and more flexibility will be possible regarding simulations. Although computationally expensive, a fully 3D simulation would be useful for providing hydrogen information in the radial, axial, and azimuthal directions simultaneously.

References

1. Duderstadt, J. Hamilton, L., *Nuclear Reactor Analysis*. 1976, Ann Arbor, MI: John Wiley & Sons, Inc.
2. Whitmarsh, C.L., *Review of Zircaloy-2 and Zircaloy-4 Properties Relevant to N.S. Savannah Reactor Design*, 1962, Oak Ridge National Laboratory.
3. Lemaignan, C. and A.T. Motta, *Zirconium Alloys in Nuclear Applications*, in *Materials Science and Technology, A Comprehensive Treatment*, B.R.T. Frost, Editor. 1994, VCH: New York. p. 1-51.
4. Sabol, G.P., *ZIRLO - An alloy development success*. Zirconium in the nuclear industry: 14th international symposium, 2005. **ASTM STP 1467**: p. 3-24.
5. Garner, G., Mardon, J., *Alloy M5 in action*, Nuclear Engineering International, 2002. **47(578)**: p. 36-37.
6. Coleman, C.E. and D. Hardie, *The hydrogen embrittlement of alpha-zirconium review*. Journal of the Less Common Metals, 1966. **11**: p. 168-185.
7. Clayton, J.C., *Cladding corrosion and hydriding in irradiated defected Zircaloy-4 fuel rods*. Corrosion, 1989. **45 (12)**: p. 996-1002.
8. Sawatzky, A. *Hydrogen in Zircaloy-2: Its distribution and heat of transport*. Journal of Nuclear Materials, 1960. **4**: p. 321-328.
9. Courty, Olivier. *Hydrogen Distribution in Zircaloy under a Temperature Gradient: Modeling, Simulation and Experiment*. Master's Thesis in Nuclear Engineering, The Pennsylvania State University, 2013.
10. Kearns, J.J., *Diffusion Coefficient of Hydrogen in Alpha Zirconium, Zircaloy-2 and Zircaloy-4*. J. Nuclear Materials, 1972. **43**: p. 330-338.
11. Bruce F. Kammenzind, D.G.F., H. Richard Peters and Walter J. Duffin, *Hydrogen Pickup and Redistribution in Alpha-Annealed Zircaloy-4*. Zirconium in the Nuclear Industry: 11th International Symposium, 1996. **ASTM STP 1295**: p. 338-370.
12. Geelhood, K.J., W.G. Luscher, and C.E. Beyer, *FRAPCON-3.4: Integral Assessment*, 2011, Pacific Northwest National Laboratory. **7022(2)**
13. Billone, M., et al., *Cladding Embrittlement During Postulated Loss-of-Coolant Accidents*, 2008, NRC. **6967**
14. Zhang, J.-H., "Hydruration du Zircaloy-4 et étude de la distribution de l'hydrogène dans une gaine de combustible REP," PhD thesis Thesis in Departement de Mecanique et de technologie, Commissariat à l'Énergie Atomique, 1993.
15. Kearns, J.J., *Terminal solubility and partitioning of hydrogen in the alpha phase of zirconium, Zircaloy-2 and Zircaloy-4*. Journal of Nuclear Materials, 1967. **22(3)**: p. 292-303.
16. McMinn, A., E.C. Darby, and J.S. Schofield, *The terminal solid solubility of hydrogen in zirconium alloys*. Zirconium in the Nuclear Industry: Twelfth International Symposium, **ASTM STP 1354**, 2000: p. 173-195.
17. Xu, J. and S.Q. Shi, *Investigation of mechanical properties of epsilon-zirconium hydride using micro- and nano-indentation techniques*. Journal of Nuclear Materials, 2004. **327**: p. 165-170.
18. Pan, Z.L., I.G. Ritchie, and M.P. Puls, *The terminal solid solubility of hydrogen and deuterium in Zr-2.5Nb alloys*. Journal of Nuclear Materials, 1996. **228**: p. 227-237.
19. Marino, G.P., *HYDIZ: A 2-dimensional computer program for migration of interstitial solutes of finite solubility in a thermal gradient (LWBR Development Program)*, in *AEC Research and Development Report - WAPD-TM-11571974*.
20. Daum, R.S., et al., *Radial-hydride Embrittlement of High-burnup Zircaloy-4 Fuel Cladding*. Journal of Nuclear Science and Technology, 2006. **43(9)**: p. 1054-1067.

21. Courty, Olivier; Motta, Arthur; Hales, Jason (INL). *3-Dimensional simulation of hydrogen diffusion and precipitation in Zircaloy-4 fuel cladding*. Journal of Nuclear Materials, 2014. **452**: p. 311-320.
22. Davis, Ian; Courty, Olivier; Avramova, Maria; Ivanov, Kostadin; Motta, Arthur. *High-Fidelity Multi-Physics Coupling for Prediction of Anisotropic Power and Temperature Distributions in Fuel Rod: Impact on Hydride Distribution*. NURETH-15 Conference Proceedings. May 2013. **49**:p.
23. Davis, Ian. *High-Fidelity Multi-Physics Coupling For Prediction of Anisotropic Power and Temperature Distribution in Fuel Rod: Impact on Hydride Distribution*. Master's Thesis in Nuclear Engineering, The Pennsylvania State University, 2013.
24. Garde, A., Smith, G., Pirek, R., *Effects of hydride precipitate localization and neutron fluence on the ductility of irradiated Zircaloy-4*, 11th International Symposium on Zirconium in the Nuclear Industry, ASTM STP **1295**, (1996), p. 407–430.
25. Salko, R.K. and M.N. Avramova, *CTF Theory Manual*, 2014, Pennsylvania State University.
26. Kochunas, B., Hursin, M., Downar, T., *DeCART-v2.05 Theory Manual*, 2009, University of Michigan.
27. *BISON Theory Manual: The Equations behind Nuclear Fuel Analysis*, 2014, Idaho National Laboratory.
28. Williamson, R.L., Hales, J.D., Novascone, S.R., Tonks, M.R., Gaston, D.R., Permann, C.J., Andrs, D, Martineau, R.C., *Multidimensional multiphysics simulation of nuclear behavior*. Journal of Nuclear Materials, 2012. **423**: p. 149-163.